International Journal of Heat and Fluid Flow 29 (2008) 703–720

Contents lists available at ScienceDirect

International Journal of Heat and Fluid Flow

journal homepage: www.elsevier.com/locate/ijhff

Shearless and sheared flow past a circular cylinder: Comparative analysis by means of LES

Takeshi Omori [a,1], Suad Jakirlić [a,*], Cameron Tropea [a], Shinnosuke Obi [b]

[a] Chair of Fluid Mechanics and Aerodynamics, Darmstadt University of Technology, Petersenstrasse 30, D-64287 Darmstadt, Germany
[b] Department of Mechanical Engineering, Keio University, Hiyoshi 3-14-1, Kohoku-ku, Yokohama 223-8522, Japan

ARTICLE INFO

Article history:
Received 11 November 2007
Received in revised form 5 March 2008
Accepted 8 March 2008

Keywords:
LES
Cylinder flow
Mean shear influence
Wake structure visualization
Re-stress energy budgets
Re-stress anisotropy
Lift forces

ABSTRACT

Large eddy simulation (LES) of the uniform shear flow past a circular cylinder at Reynolds number $Re_D = 3900$ with increasingly enhanced mean shear magnitude $|du_F/dy|$ corresponding to the shear rate ($SR = |du_F/dy|D/u_F$) range between 0 (shearless flow) and 0.177 have been performed in order to provide a basis for comparative analysis of the shear-induced effects with respect to the structural characterization of the cylinder wake. The case characterized by the velocity gradient being perpendicular to the cylinder axis was considered. In addition to the direct comparison of the present computational results with the reference database (mean velocity and Reynolds stress profiles at selected locations in the near and the far wake), the results presentation includes pressure field around the cylinder, mean pathlines inside and outside the separation bubble, vortex structure visualization by the pressure fluctuations and Q-criterion as well as the Reynolds stress anisotropy evolution and energy budgets of the Reynolds stress components and the kinetic energy of turbulence. An important outcome arising from the present computational study relates to the asymmetric shape of the mean quantity profiles with the local maxima/minima shifted to the high velocity side, indicating a strong modulation of the large-scale structures in the wake due to the imposed mean shear. It applies especially to the far wake region. Here, the structures illustrated by the fluctuating pressure field clearly show their existence only on the high velocity side. In contrast, the small-scale structures remain almost unaffected by the mean shear. Evaluation of the lift forces from the velocity and pressure fields illustrate an increasing magnitude with the shear rate towards the lower velocity side, in good agreement with corresponding experiments.

1. Introduction

One of the most frequently investigated flow configurations in fluid mechanics research is the flow past a circular cylinder, being also one of the most important examples of bluff bodies. Because of its fundamental importance (it represents a generic configuration for studying vortex dynamics, the drag and lift variation due to wake unsteadiness, etc.) and its relevance in technical applications this flow has been intensively investigated in the past, see e.g. Roshko (1954) and a review of early works on this topic in Hinze (1975) and Schlichting (1979), as well as more recent computational studies, e.g., Beaudan and Moin (1994), Breuer (1998), Travin et al. (1999) and Kravchenko and Moin (2000). In all of these studies, the oncoming flow was uniform, i.e. with no mean shear imposed. However, in practical engineering situations, flow configurations where the oncoming flow exhibits a strong velocity gradient are more likely encountered. This is especially valid if the cylinder is situated in the wall boundary layer, which inherently exhibits strong velocity variation and a lower local Reynolds number. The present work deals with such a situation, where the vortex shedding from a circular cylinder in a linear shear flow with the velocity gradient being normal to the cylinder axis is considered, Fig. 1.

Such flow configurations are encountered in civil engineering field, where a cylindrically formed objects[2] are situated in the earth boundary layer, exhibiting a strong mean velocity gradient. The configuration investigated in the present study is very similar to the recent experimental study of Cao et al. (2007) with a linear shear flow past a circular cylinder, providing the variation of the Strouhal number, mean and fluctuating base pressures and drag and lift forces in terms of the shear rate (the range between SR = 0.0–0.27 is covered; $SR = |du_F/dy|D/u_F$). The Reynolds number range considered in this study is $Re_D = 17{,}000$–$36{,}000$, corresponding to the upper (lower)

* Corresponding author. Tel.: +49 6151 163554; fax: +49 6151 164754.
E-mail address: s.jakirlic@sla.tu-darmstadt.de (S. Jakirlić).
[1] Graduate School of Engineering, Department of Mechanical Engineering, Osaka University, Yamadaoka 2-1, Suita-shi, 565-0871 Osaka, Japan.

[2] A large number of experimental and computational studies of the shearless and shear flow past a square cylinder have been reported in the literature. We mention here only a few related studies, e.g. Rodi et al. (1997), Cheng et al. (2005) and Luo et al. (2007).

0142-727X/$ - see front matter © 2008 Elsevier Inc. All rights reserved.
doi:10.1016/j.ijheatfluidflow.2008.03.012

Nomenclature

D	cylinder diameter
E^*_{11}	one-dimensional energy spectra of the streamwise velocity fluctuations, $E^*_{11} = E_{11}/U^2_\infty$
f_{st}	Strouhal frequency
k_z	wavenumber with respect to the spectra evaluation in spanwise direction
p	instantaneous pressure field
Re_D	Reynolds number, $Re_D = U_\infty D/\nu$
S_{ij}	instantaneous strain rate, $S_{ij} = 0.5(\partial u_i/\partial x_j + \partial u_j/\partial x_i)$
$\lvert S\rvert$	strain rate magnitude, $\lvert S\rvert = \sqrt{2S_{ij}S_{ij}}$
SR	shear rate parameter, SR = $\alpha D/u_F$
St	Strouhal number, $St = f_{st}D/U_\infty$
u_i	instantaneous velocity field
u_F	velocity of the oncoming flow at the cylinder centerline $y = 0$, $u_F \equiv U_\infty$
U, V	streamwise and crossflow mean velocity components

Greek letters

α	mean shear intensity, $\alpha = \lvert du_F/dy\rvert$ (Fig. 1)
Δ_i	grid spacing in each coordinate direction ($i = x,y,z$)
$\overline{\Delta}$	filter width, $\overline{\Delta} = \sqrt[3]{\Delta x\Delta y\Delta z}$
ν	kinematic viscosity
ν_t	(or ν_{SGS}) turbulent viscosity of residual (SGS) motion
Ω_{ij}	instantaneous vorticity, $\Omega_{ij} = 0.5(\partial u_i/\partial x_j - \partial u_j/\partial x_i)$

Superscripts

a	deviatoric part
+	normalized with wall units U_τ and ν/U_τ; $U_\tau = \sqrt{\tau_w/\rho}$
φ'	fluctuation ($=\varphi - \langle\varphi\rangle$)

Other symbols

$\overline{\varphi}$	filtered value
$\langle\varphi\rangle$	Reynolds-averaged (in time) value

Abbreviations

SGS	subgrid-scale
GS	grid-scale

limit of the middle (high) subcritical range of a disturbance-free flow past a circular cylinder according to Zdravkovich (1997). Cao et al. provided also a review of the relevant publications in this field. Besides the flow configuration considered in the present work, the bluff body aerodynamics is often investigated under conditions of the mean shear being aligned with the body axis. Examples of such investigations are reported in Tavoularis et al. (1987), Woo et al. (1989) and Parnaudeau et al. (2007). In addition to the spanwise shear, the effects of the spanwise non-uniformity in cylinder diameter was also investigated in the latter publication.

Another important application in which a shear flow past a bluff body is encountered is with a dispersed phase in a two-phase flow, e.g. Saffman (1965, 1968) and McLaughlin (1991). Here, the shear-induced lift forces acting on a spherical particle are the prime concern. The resulting lift force formulations were derived for a particle in a linear shear flow away from walls, under the strict constraint that the Reynolds number is smaller than unity. Analysing these and some other solutions derived by previous investigators (e.g. McLaughlin, 1993), Wang et al. (1997) proposed an optimum formulation for the lift force on a particle in a wall-bounded shear flow and validated its performance in the framework of LES predicting particle deposition in a vertical turbulent channel flow. Akagawa et al. (1989) and Sakaguchi et al. (1991) observed in their solid–liquid upward duct flow experiments that the spherical particles tend to concentrate near the side walls or in the duct core, depending on the flow conditions. This behaviour cannot be explained with classical lift force models, such as the models of Saffman (1968) or Mei (1992), which always yield the shear-induced lift force towards the duct core being characterized by higher velocity values (direction of positive velocity gradient). These experiments were all conducted at low volume fractions, where particle interactions do not seem to be the major cause of the observed behaviour. In the experimental study by Moraga et al. (1999; $Re_D \leqslant 17{,}000$; SR = 0.0–0.177) it was demonstrated that the lift force on a sphere has a strong dependence on the Reynolds number and the mean shear intensity of the oncoming flow. This work highlighted an interesting phenomenon with respect to the change of the lift coefficient sign, from positive to negative, within the shear parameter range investigated. It was observed that under these conditions, where massive separation takes place, the wake structure influences decisively the forces acting on cylinder.

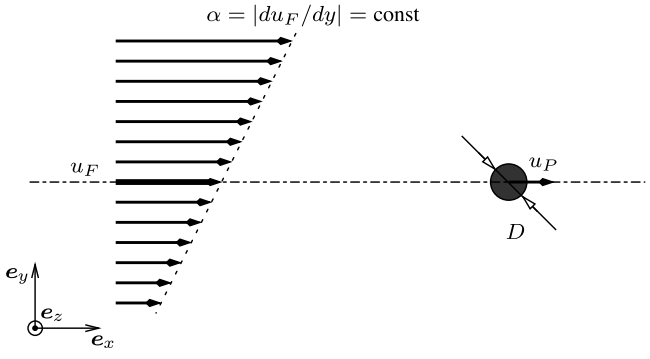

Fig. 1. Schematic of the considered flow and the coordinate system.

The latter motivated the present fundamental study of wake structure characterization. The negative lift force acting from the higher velocity side towards the lower velocity side was also observed in the experiments of Sumner and Akosile (2003; performed in the subcritical Reynolds number range $40{,}000 \leqslant Re_D \leqslant 90{,}000$ and the shear rate range $0.02 \leqslant \text{SR} \leqslant 0.07$) and Cao et al. (2007) of linear shear flow past a circular cylinder for the entire range of the operating conditions. A circular cylinder (Fig. 1) is considered also in the present work. The adopted Reynolds number based on the bulk velocity of the oncoming flow and the cylinder diameter was $Re_D = 3900$. This value corresponds to the subcritical regime being characterized by the laminar-turbulent transition in the separated shear layer. This Reynolds number was chosen because of the extensive reference database for the shearless case, both experimental and computational (LES and DNS), e.g. Lourenco and Shih (1993), Ong and Wallace (1996), Mittal and Moin (1997), Breuer (1998), Kravchenko and Moin (2000) and Tremblay (2001). Among others, this case serves also to choose the adequate solution domain (shape and size) and to perform a grid study in order to minimize the uncertainties arising from the spatial and temporal resolutions. An extensive analysis of the quality assessment measures has been provided as well as a detailed comparison with other studies. The investigated range of the shear parameter, $0 \leqslant \text{SR} \leqslant 0.177$, was selected in order to cover the conditions investigated experimentally by Moraga et al. (1999), Sumner and Ako-

sile (2003) and Cao et al. (2007). It should be noted that both Moraga et al. and Cao et al. varied not only the shear intensity but also the Reynolds number. In the present analysis, we varied solely the shear intensity in order to obtain the shear parameter range of interest. This is namely the flow situation, where the wake effects on the lift coefficient become dominant over the inviscid effects causing the sign change (from positive to negative) of the lift coefficient.

2. Computational method

All simulations were performed with the computer code FAST-EST (2005) which is based on a finite volume numerical method for solving three-dimensional, filtered Navier–Stokes equations on block-structured, body-fitted, nonorthogonal meshes. Block interfaces are treated in a conservative manner, consistent with the treatment of inner cell faces. A cell centered (collocated) variable arrangement and Cartesian vector and tensor components are used. The well-known SIMPLE algorithm for the collocated variable arrangement was applied for coupling the velocity and pressure fields. The convective transport of all variables was discretized by a second-order central differencing scheme (CDS), implemented in the so-called deferred-correction-approach manner. It should be emphasized here that the values of all relevant variables and terms are obtained by accounting for 100% of the CDS in this blending procedure. In such a way the second-order accuracy of the method could be maintained. It is well known that any fraction (even very small one) of an upwind-biased scheme can cause damping of the small-scale structures and lead to the increase of the turbulent viscosity level of the large scales. The best proof that our simulations were not contaminated by applying the deferred correction approach is the ratio of the SGS viscosity to molecular viscosity (displayed subsequently in Fig. 5), which was indeed very small, substantially under one for the grids B and C. Time discretization was accomplished applying the second-order (implicit) Crank–Nicolson method. The filtered Navier–Stokes equations governing the incompressible, unsteady flow past a circular cylinder read:

$$\frac{\partial \overline{u}_i}{\partial x_i} = 0 \tag{1}$$

$$\frac{\partial \overline{u}_i}{\partial t} + \overline{u}_j \frac{\partial \overline{u}_i}{\partial x_j} = -\frac{1}{\rho}\frac{\partial \overline{p}}{\partial x_i} + \frac{\partial}{\partial x_j}(2\nu \overline{S}_{ij} - \tau_{ij}) \tag{2}$$

The quantity $\tau_{ij}(=\overline{u_i u_j} - \overline{u}_i \overline{u}_j)$, called SGS (subgrid-scale) stress tensor, being the consequence of the filtering procedure, has to be determined by an SGS model. In the present work the most widely used model formulation due to Smagorinsky based on the eddy viscosity assumption is used:

$$\tau_{ij}^a = \tau_{ij} - \delta_{ij}\frac{\tau_{kk}}{3} = -2\nu_t \overline{S}_{ij} \tag{3}$$

The subgrid-scale viscosity ν_t is given by a mixing length-based model

$$\nu_t = (C\overline{\Delta})^2 |\overline{S}| \tag{4}$$

with $|\overline{S}| = \sqrt{2\overline{S}_{ij}\overline{S}_{ij}}$ and $\overline{\Delta} = \sqrt[3]{\Delta x \Delta y \Delta z}$ representing the velocity $(C\overline{\Delta}|\overline{S}|)$ and length scales $(C\overline{\Delta})$ of the residual (SGS) motion. The model coefficient C was either set to the constant value 0.1 or was dynamically determined by the procedure proposed by Germano et al. (1991) and Lilly (1992). No damping of the turbulent viscosity by approaching the solid wall, such as the one proposed by van Driest modelled in terms of the non-dimensional wall distance y^+ ($y^+ = y U_\tau/\nu$) was applied in conjunction with the Smagorinsky model, because of the known uncertainties in regions affected by separation and reattachment, where the wall shear stress ($\tau_w = \rho U_\tau^2$) approaches the value zero. In any case the focus in the present work was on the dynamic procedure of the coefficient determination in the model formulation for the SGS viscosity. All important conclusions are based on the results obtained with this dynamic model.

2.1. Computational details

The solution domain adopted was meshed with a block-structured grid, whose topology is displayed in Fig. 2. Three different grids consisting of approximately 670,000 (grid A), 1.1 million (grid B) and 2.2 million cells (grid C) were used to investigate uncertainties arising from the grid quality. Table 1 gives an overview about

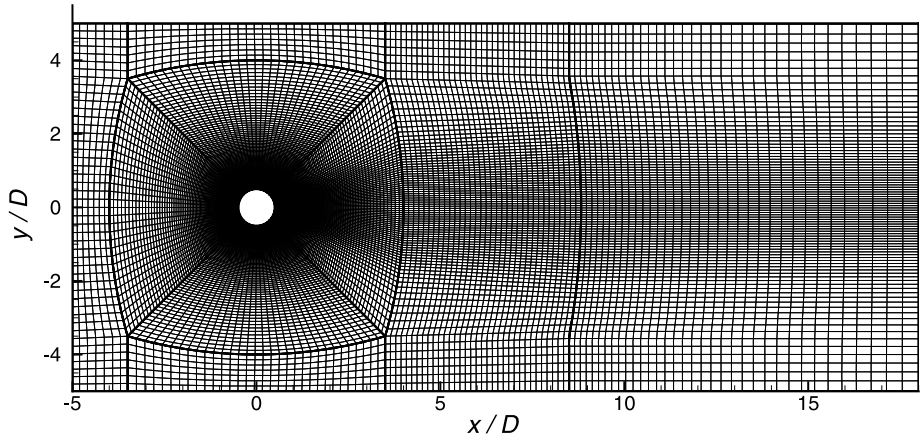

Fig. 2. Block and cell distribution for grid B in the x–y-plane.

Table 1
Summary of the grid characteristics

Grid	No. of grid cells ($x-y$,z)	Domain $L_x \times L_y \times L_z$	Near-wall resolution $(\Delta x^+_{max}, (\Delta y^+/2)_{max}, \Delta z^+_{max})$	$(\overline{\Delta}/\eta)_{max}$
A	$21{,}043 \times 32$	$(-8D, 15D) \times (-5D, 5D) \times (0, \pi D)$	(20,0.32,81)	45.5
B	$34{,}100 \times 32$	$(-5D, 18D) \times (-5D, 5D) \times (0, \pi D)$	(23,0.32,78)	20.2
C	$34{,}100 \times 64$	$(-5D, 18D) \times (-5D, 5D) \times (0, \pi D)$	(23,0.32,40)	17.6

the solution domain dimensions with respect to the position of the domain boundaries and appropriate grid resolutions in all three coordinate directions. The influence of the position of the inlet plane was also examined. The velocity profiles obtained at $x/D = -0.5$ collapse into a single curve (not shown here). Fig. 2 shows the plane view of the second finest grid (B), which has higher resolution in the wake region than the coarsest grid (A). The finest grid (C) has the same resolution in the x–y-plane as the grid B but doubled the number of grid cells in the spanwise direction. The computational domain was uniformly meshed in the spanwise direction for all three grids. Both spanwise dimension and spanwise resolution are in line with reference LES simulations, e.g. with those performed by Kravchenko and Moin (2000) and Breuer (1998). In the work of Breuer an O-type grid with domain radius up to 15D was used (let us recall that our outlet boundary was positioned at the same distance from cylinder), enabling a larger solution domain in cross direction and especially in front of the cylinder, but maintaining similar grid resolution. The total number of grid points was approximately the same. Contrary to the grid size around the cylinder itself and in the near wake, which was of the comparable resolution, the far wake was meshed by somewhat more grid cells in the work of Breuer. These circumstances can explain to some extent the differences between the present and reference computational results (see Section 3). No-slip

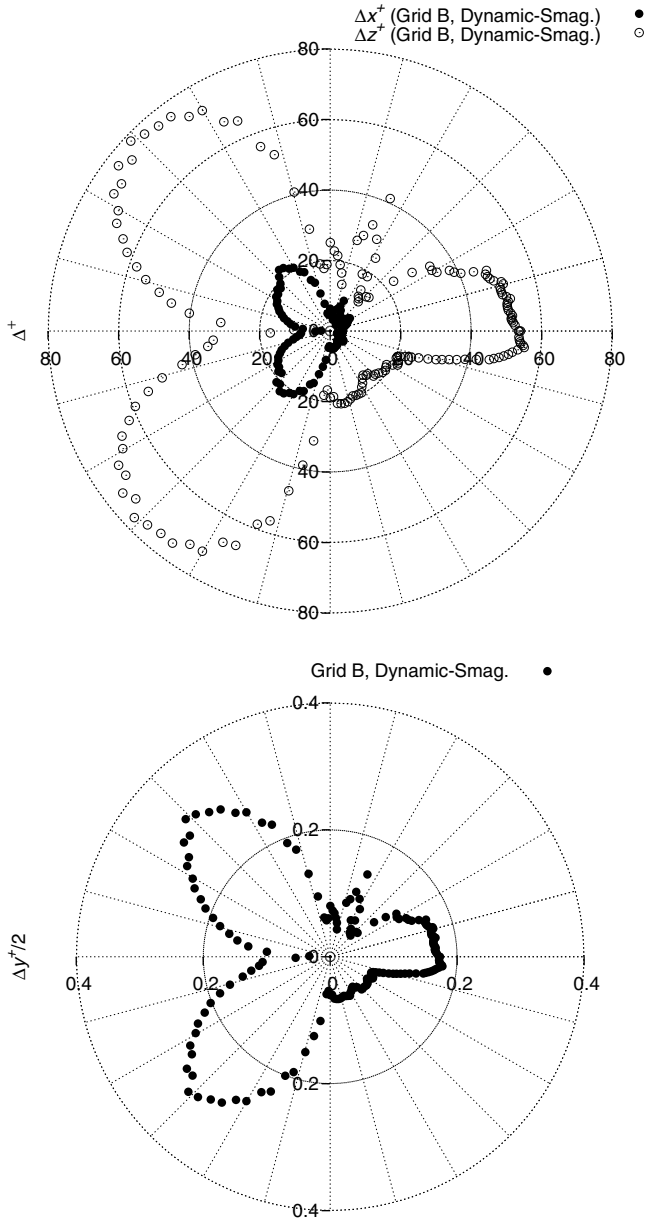

Fig. 3. Near-wall resolution for the grid B (SR = 0).

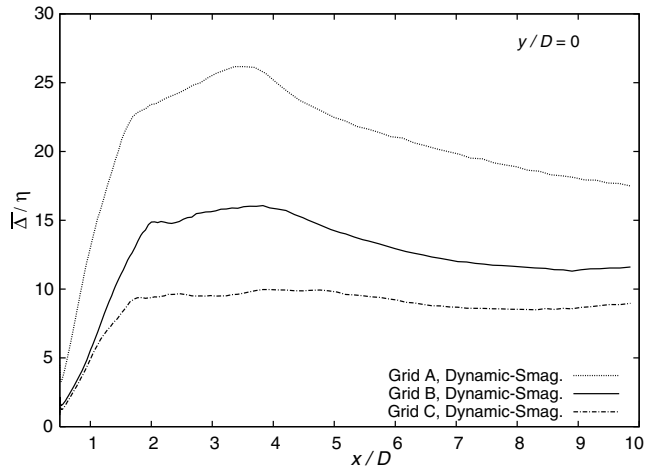

Fig. 4. Variation of the filter width normalized by Kolmogorov length along the centerline in the cylinder wake (SR = 0).

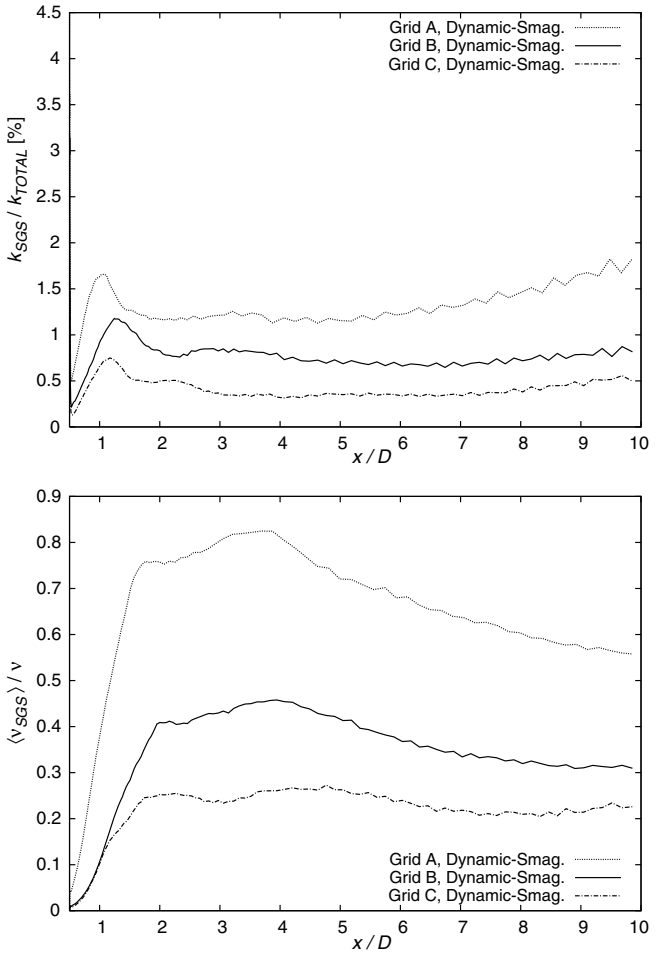

Fig. 5. Variation of k_{SGS}/k_{total} and ν_{SGS}/ν along the centerline in the cylinder wake (SR = 0).

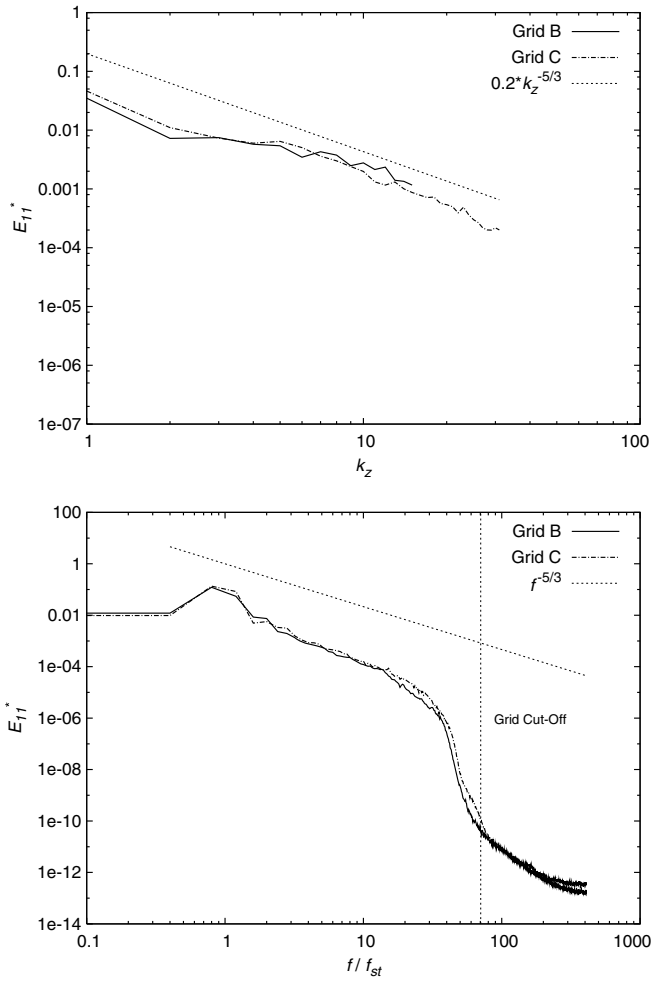

Fig. 6. One-dimensional wave-number (upper) and frequency spectra (lower) in the wake (the vertical line shows the grid cut-off), SR = 0.

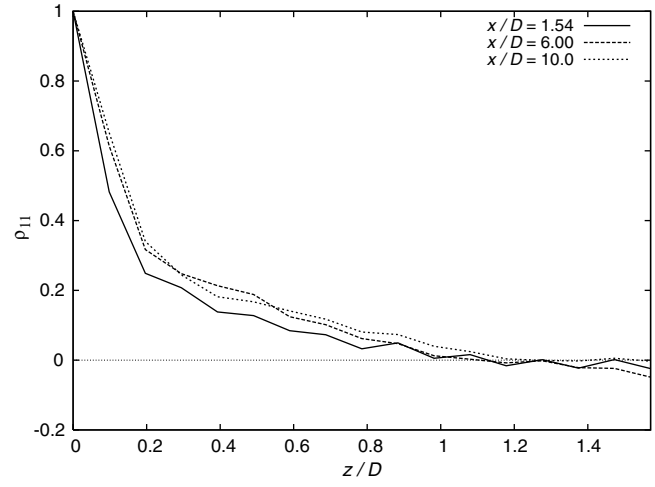

Fig. 7. Autocorrelation of the streamwise velocity fluctuations at three locations in the wake (grid B, SR = 0).

boundary conditions were applied on the cylinder surface and integration up to the wall was performed. The periodicity of the flow was assumed in the spanwise direction of the domain. At the inlet plane no perturbations were added to the mean velocity profile. The convective boundary conditions given by

$$\frac{\partial u_i}{\partial t} + U_\infty|_{y=0}\frac{\partial u_i}{\partial x} = 0 \tag{5}$$

were imposed at the outflow plane, the convective velocity corresponding to the mean streamwise velocity U_∞ of the bulk flow taken at the centerline ($y = 0$).

The statistics were accumulated over a period of at least 12 vortex shedding cycles (in most cases the sampling period corresponded to 30 vortex shedding cycles). The spatial averaging was accomplished in the statistically homogeneous spanwise direction. The statistics were monitored at a point placed in the separated shear layer behind the cylinder after every time step and were considered to be converged to the uncertainty of a few percent. The free-stream velocity based CFL number ($=u\Delta t/\Delta x$), representing the time step chosen, did not exceed unity in the entire solution domain for the grids B and C. Further time step refinement corresponding to the $CFL \approx 0.5$ did not result in any noticeable change of the solution. In the case of the coarsest grid, the maximum CFL number was about 2.

The near-wall grid resolution has been chosen such that the laminar boundary layer at the windward side is properly resolved. The boundary-layer thickness at the curved cylinder surface was estimated to be $\delta \approx 0.05D$ at $\theta = 90°$ measured from the stagnation point denoted by $\theta = 0°$ (Tremblay, 2001). This is obtained by adopting the well-known formulation for the flat plate boundary layer and assuming negligible curvature effects. Accounting for the surface curvature causing a certain flow acceleration would yield a somewhat thinner boundary layer. The size of the wall closest cell face in the radial direction is $0.000788D$. Such a boundary-layer thickness accommodates up to 40 grid cells taking into account the grid expansion factor of 1.032. The number of grid cells covering the wall region in which the mean velocity field reaches the maximum value on the windward side amounts to 22 (this position corresponds approximately to $0.025D$ at $\theta = 45°$). Fig. 3 displays the near-wall resolution of the grid B at $z = \pi D/2$, expressed as the size of the wall adjacent cells normalized by the local instantaneous friction velocity. The grid spacing reaches its maximum at 45°, where the flow around the cylinder exhibits the strongest acceleration. Unlike the windward face, substantial asymmetry is observed on the leeward side. The constellation shown in Fig. 3 corresponds to the time sequence where the instantaneous separation point at the lower half surface is shifted forward compared to the separation at the upper half surface. Similar values for Δx^+, Δy^+ and Δz^+ are obtained for other time sequences. The maximum values of the grid spacing in all three coordinate directions are listed in Table 1 along with those for the other two grids. Although it is not applicable here (the flow on the windward face is laminar and on the rear of the cylinder the flow is separated) let us just recall that the reference grid resolution for attached turbulent boundary layers estimated by Piomelli and Chasnov (1996) requires the values $\Delta x^+ < 50$ (at most 150), $\Delta y^+ < 2$, $\Delta z^+ < 15$ (at most 40). The near-wall grid resolution pertinent to the grid B corresponds to $\Delta x^+ = 23$, $\Delta y^+ = 0.64$ and $\Delta z^+ = 78$ (Table 1). Further grid refinement by doubling the number of the cells in the z-direction (grid C) led to $\Delta z^+_{\max} = 40$. However, it was not of decisive importance with respect to the final results, as will be seen when presenting other quality assessment measures in reminder of this section.

One of the important measures for the grid quality assessment is the ratio of the representative grid-scale $\overline{\Delta}$ to the Kolmogorov length scale η. Fig. 4 depicts its variation along the centerline behind the cylinder. The maximum values of this normalized filter width in the entire solution domain is listed in Table 1. The Kolmogorov length scale $\eta(=(\nu^3/\epsilon)^{\frac{1}{4}})$ was evaluated from the Reynolds averaged value of the dissipation rate as follows:

$$\epsilon \approx \epsilon_{GS} - \mathscr{T}_{GS} = 2\nu\overline{S}_{ij}\overline{S}_{ij} - \tau^{a}_{ij}\overline{S}_{ij}, \quad (6)$$

Here, ϵ_{GS} and $\mathscr{T}_{GS}$ represent the dissipation rate at the grid-scale (GS) and the energy transfer rate from the grid-scale to the sub-grid-scale, respectively. Ideally, the filter width should be placed well in the inertial subrange, which spreads roughly over one non-dimensional frequency decade ($10^0 \leqslant f/f_{St} \leqslant 10^1$) at this low Reynolds number according to the experimentally obtained frequency spectra at several locations on the centerline in the cylinder wake (Ong and Wallace, 1996). The maximum values of the characteristic filter width corresponding to both grids B and C, shown in Table 1, are $(\overline{\Delta}/\eta)_{max} = 20.2$ and 17.6, respectively. These values correspond to the shear-layer region. However, the filter width variations in the cylinder wake along the centerline indicate the grid resolution being even higher, Fig. 4. Let us recall the constraint $\overline{\Delta}/\eta = 10-12$ being valid for the fully-developed isotropic turbulence (Pope, 2000). Although not entirely representative for the shear-layer region exhibiting anisotropy, it could still be used for analysing the grid resolution. The Kolmogorov length is generally smaller (higher viscous dissipation rate of the kinetic energy of turbulence) in the anisotropic flow regions compared to the isotropic ones. It would lead to the higher values of this non-dimensional filter width by keeping the grid spacing $\overline{\Delta}$ constant. Accordingly, the grid spacing adopted here would be closer to such a criteria. The suitability of the adopted grid resolutions for LES is further checked by analysing the SGS fractions of turbulent kinetic energy and turbulent viscosity, Fig. 5. These figures display the SGS contribution to total turbulence kinetic energy and the ratio of turbulent SGS viscosity to molecular viscosity along the centerline behind the cylinder. This analysis shows a minor contribution to the total k-value (less than 1%) for both grids B and C. The modelled SGS kinetic energy is estimated as $k_{SGS} = \nu_t|\overline{S}|/0.3$ (Mason and Callen, 1985). The employed resolution maintains the ratio ν_{SGS}/ν under 0.5.

The one-dimensional spatial and temporal spectra of the streamwise velocity fluctuations, shown in Fig. 6, were measured at the position $(x/D, y/D) = (1.54, 0.5)$ for approximately five vortex shedding cycles. A regular decay of slope close to $-5/3$ is observed and the inertial subrange is well resolved, which is essential for a successful LES computation. The one-dimensional wave number spectra (Fig. 6, upper) obtained at grid B is characterized by a somewhat higher energy level over the resolvable inertial subrange corresponding to $5 \leqslant k_z \leqslant 15$ compared to the grid C. The resolvable wave number range pertinent to the grid C follows the $k_z^{-5/3}$ range for about one decade. It should be noted that the sampling rate corresponding to the chosen time step width ($f/f_{st} \approx 400$, Fig. 6) is higher than the grid cut-off frequency f_c (depicted as the vertical line in Fig. 6; $f_c = U/\Delta x$ at $(x/D, y/D) = (1.54, 0.5)$), the latter denoting the maximal resolvable frequency on the adopted grid in accordance with the streamwise spacing and Taylor's hypothesis. This confirms a sufficient temporal resolution of the present simulations.

The spanwise autocorrelation functions ρ_{11}, obtained along a spanwise line within the cylinder wake at three streamwise loca-

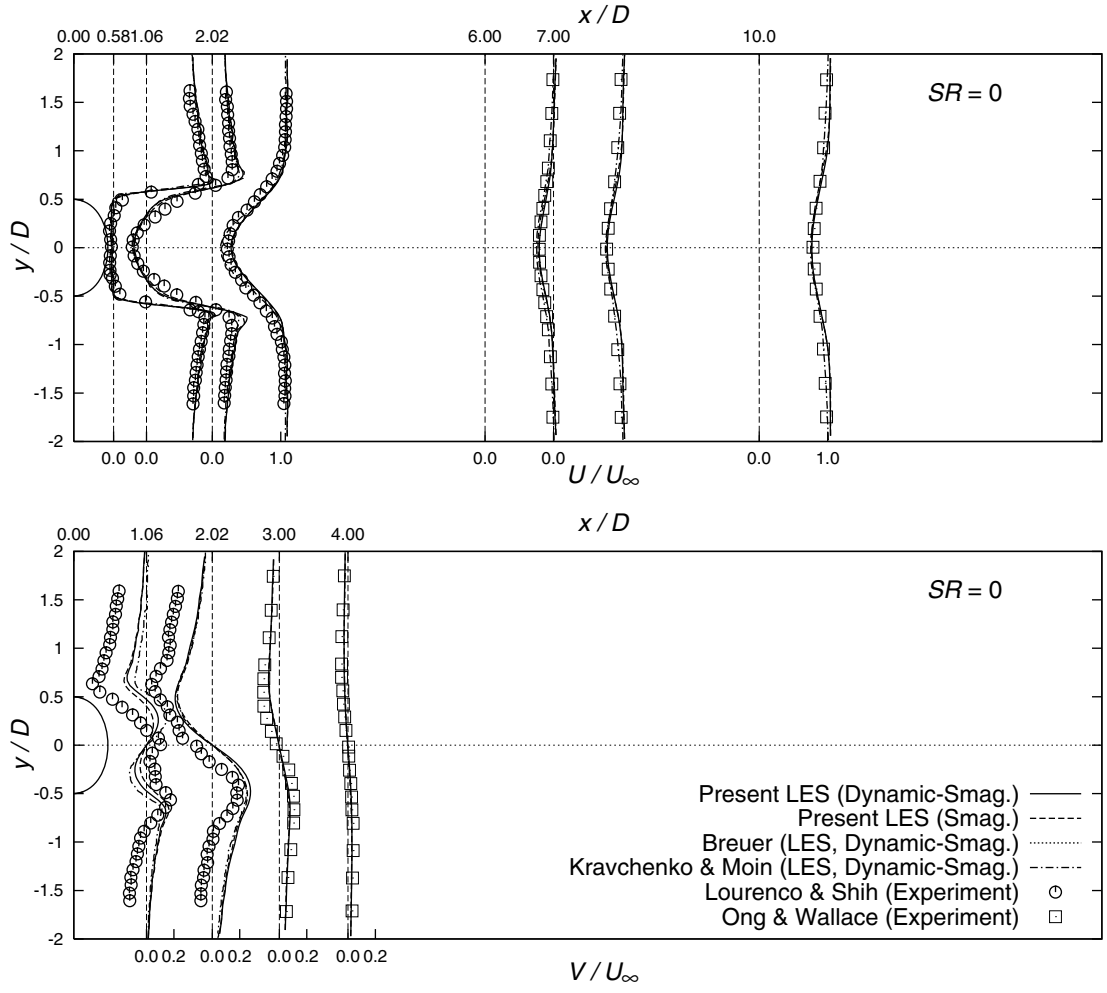

Fig. 8. Evolution of the mean axial and radial velocity profiles in the cylinder wake for SR = 0.

tions $x/D = 1.54$, 6.0 and 10.0 applying the grid B, are plotted in Fig. 7 in order to check the adequacy of the spanwise size of the solution domain. As illustrated, the autocorrelation vanishes at a distance of the half domain size, which is required to resolve the lowest possible wavenumber in the flow. The adopted domain size in the spanwise direction πD in combination with the periodic boundary conditions is therefore considered to be sufficient to ensure spanwise decorrelation.

According to the analysis performed it is concluded that the grid B can be regarded as appropriate for the present study and adopted for the subsequent simulations of the cases with the mean shear imposed on the approaching flow.

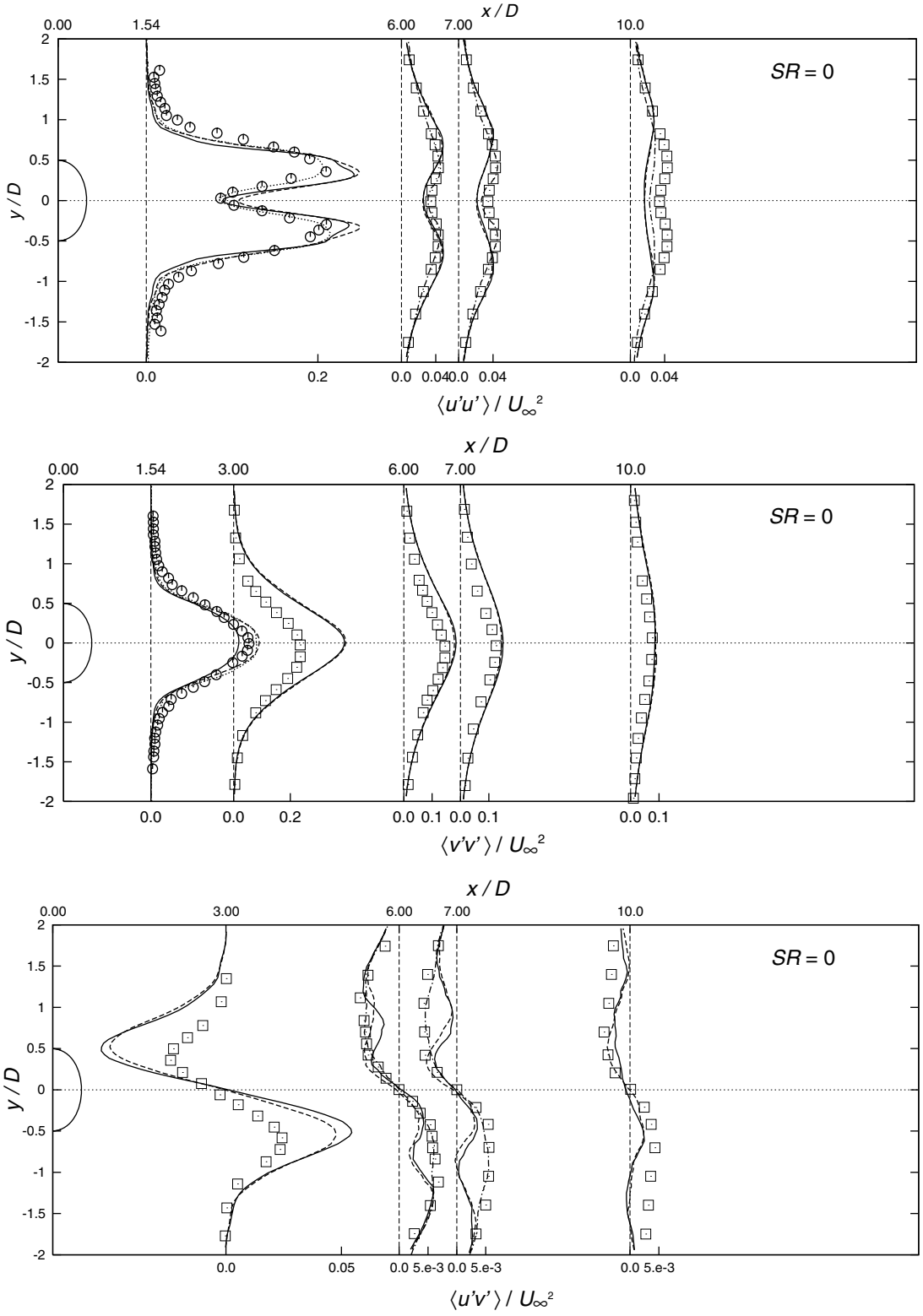

Fig. 9. Evolution of the Reynolds stress component profiles in the cylinder wake for SR = 0. Key as in Fig. 8.

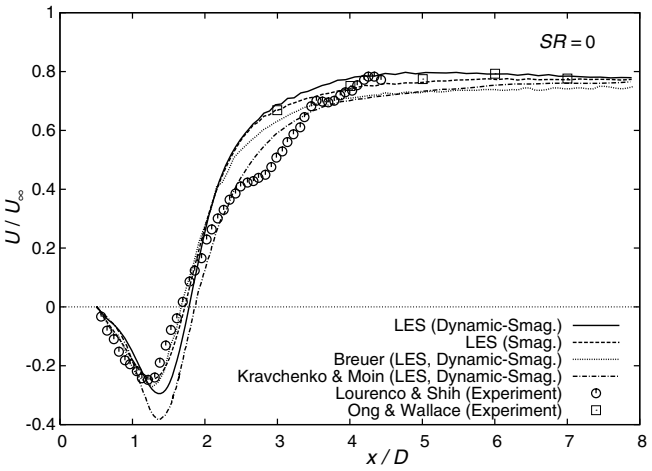

Fig. 10. Evolution of the centerline velocity in the cylinder wake for SR = 0.

3. Results and discussion

To investigate the shear effects and the corresponding wake structure on the cylinder, the simulations were conducted applying the grid B for five different shear rates SR = 0.0, 6.53×10^{-4}, 6.53×10^{-3}, 0.0918 and 0.177. The Reynolds number was kept constant ($Re_D = 3900$). The dynamic Smagorinsky model was applied as the subgrid-scale model. In the following discussions, the symbol for the filter operation $\overline{(\,)}$ is omitted for the sake of brevity. The evolution of the mean flow (velocity and pressure fields) and turbulent quantity profiles in the cylinder wake and associated Reynolds stress anisotropy evolution will be shown first for both shearless and sheared cases followed by the analysis of the mean shear influence on the terms in the transport equations of the Reynolds stress components and the structural properties in the cylinder wake.

3.1. Mean flow and turbulence evolution

Figs. 8 and 9 display the profiles of the mean velocities and the Reynolds stress components in the wake of cylinder for the shearless case (SR = 0). The velocity field exhibits a typical evolution representative of a flow past a bluff body dominated by a large recirculation zone (see also Fig. 13). The shear layers separated from the upper and lower cylinder sides join at the free reattachment point situated at the symmetry plane. This process is followed by the flow bifurcation at the reattachment. Whereas one branch flows back creating the recirculation zone, another branch contributes to the flow recovery. The Reynolds stress field indicates the highest turbulence intensity in the regions with the most intensive mean flow deformation (largest axial and radial velocity gradients; see also Figs. 19–22). In addition to the present results obtained by using both the Smagorinsky and dynamic models and available experimental data, the LES results of Breuer (1998) and Kravchenko and Moin (2000) are shown for comparison. The results for the velocity field exhibit a high level of agreement with results of reference simulations in both characteristic flow zones: flow reversal immediately behind the cylinder and recovery region. This is also visible in Fig. 10, where the centerline velocity evolution is depicted, exhibiting negative values in the separation bubble and a gradual increase until the bulk velocity is recovered. A slight deviation of the computational velocity profile from the experimental one at the position $x/D = 1.06$ in the recirculation region points out the difference in the profile shape. Whereas a *U*-shape velocity profile was obtained computationally, the experimentally detected profile exhibits a *V*-shape associated with a slightly narrower recirculation zone. Contrary, the larger length of the separation bubble corresponding to $L_r/D \approx 1.3$ is obtained computationally compared to the experimental one $L_r/D \approx 1.18$. The former corresponds to the position of the free reattachment point at $x/D \approx 1.8$. These results are in very good agreement with the LES of Kravchenko and Moin (2000). They argued that the reason for a somewhat shorter separation bubble obtained experimentally may lay in the earlier transition in the separated shear layer being caused by some external disturbances. It can to a certain extent justify the noticed departure. The computationally obtained results for the cross velocity component indicate perfectly symmetrical profiles contrary to the experiments which exhibit a certain scatter resulting in a finite velocity value at the symmetry plane. Nevertheless, the overall agreement between simulations and experiment can be considered satisfactory. However, this is not entirely the case for the Reynolds stress development. Especially affected is the shear stress component in the far wake region. The shear stress profiles at $x/D = 6$ and 7 exhibit some anomalous departure from the experimental data in the region of highest turbulence intensity, representing an unsatisfactory outcome. It is a

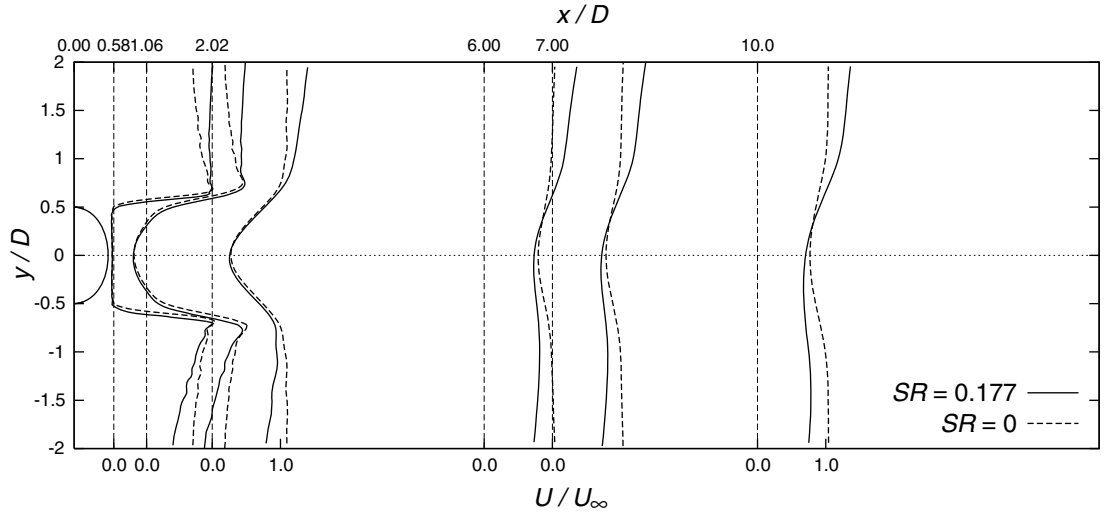

Fig. 11. Evolution of the mean axial velocity profiles in the cylinder wake for SR = 0 and SR = 0.177.

very surprising result, especially when looking at the smooth profiles of the other two Reynolds stress components. Interestingly, although not at the same location, an identically anomalous profile shape at $x/D = 10$ was obtained by Mittal and Moin (1997; displayed in Fig. 17 in the work of Kravchenko and Moin, 2000). Its origin is indeed unclear. One possible reason can be the inadequate grid refinement in this region. It should be mentioned that the grid refinement in the spanwise direction (grid C) did not contribute to

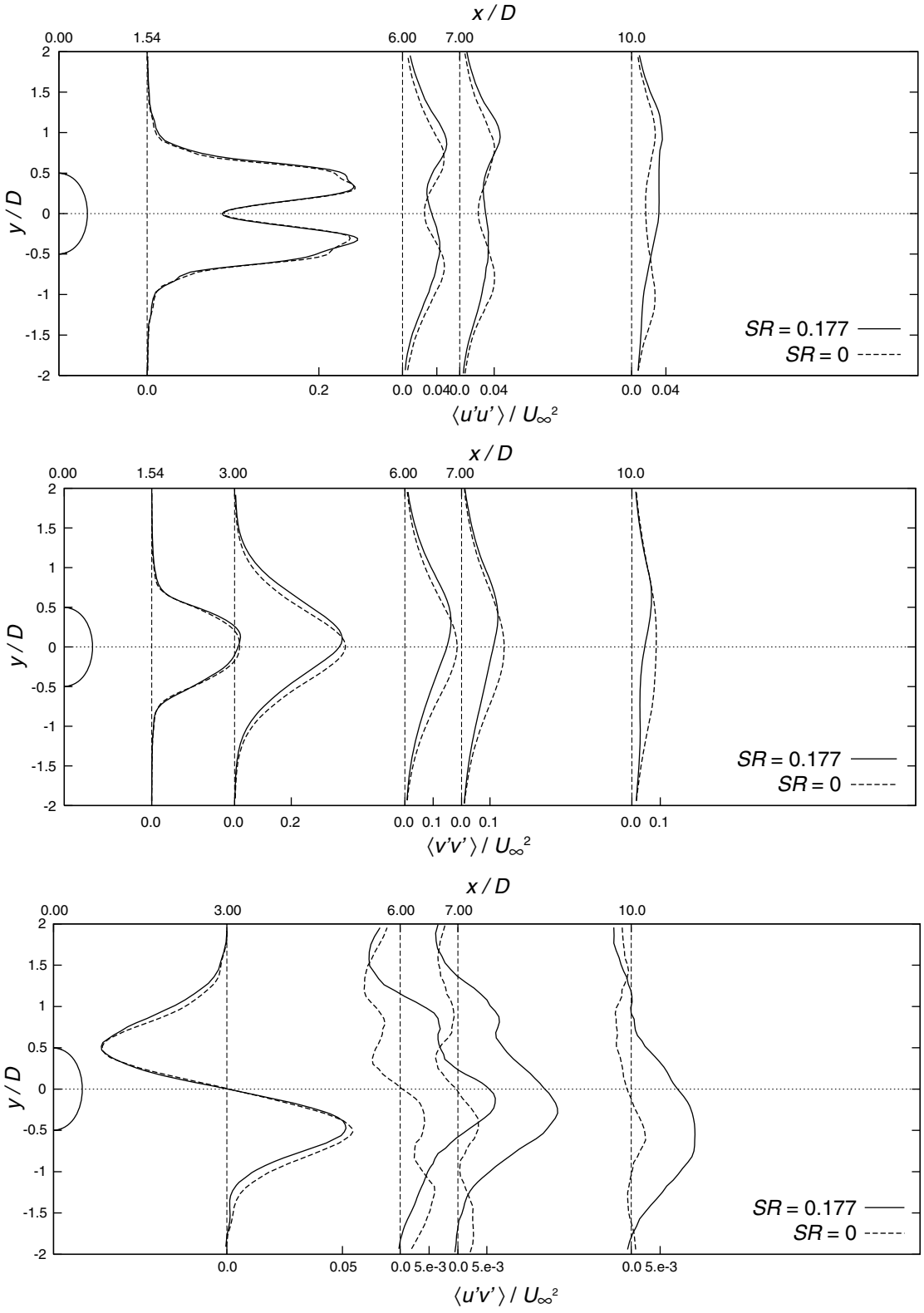

Fig. 12. Evolution of the Reynolds stress component profiles in the cylinder wake for SR = 0 and SR = 0.177.

the elimination of this anomaly. The differences between our grid design and those applied in other relevant works were discussed in the section about computational details. The cause for that can also be associated with the adopted central differencing scheme. It should be recalled, that the above mentioned result of Mittal and Moin (1997) was obtained by using the finite difference method and the second-order central differencing scheme, which was also applied in the present manuscript. The relevant discussion will be continued when analysing the results of the shear flow simulations pertinent to the Reynolds stress components and energy budgets.

Figs. 11 and 12 show the axial velocity and Reynolds stress component development in the cylinder wake corresponding to the highest considered shear rate SR = 0.177. The results obtained for the shearless case are also shown in order to emphasize the relative difference between both flow configurations. It is interesting to note that the recirculation zone was not affected by the mean shear imposed on the flow. The size of the backflow region ($L_r/D \approx 1.3$) was not changed at all. Hence, the profiles in the separation bubble retain their symmetrical shape. The effects of the shear rate imposed is noticeable in the regions above (intensification of the convective transport implies a higher level of the shear stress) and below this region and especially in the far wake. The profiles of all quantities become gradually asymmetrical towards the high velocity side. The strongest influence of the mean shear is observed at the profiles of the shear stress component $\langle u'v' \rangle$. The turbulent shear stress exhibits positive values over a wide range of the far wake. Hereby, the positive peak values are substantially higher than the negative ones. The shear stress component profiles for the shear case also exhibit similar curious dimples as in the shearless flow, although less pronounced. One should note, that the magnitude of the shear stresses is much lower (10–20 times) compared to the streamwise and normal stress components. Correspondingly, all potential errors arising in the Reynolds stress evaluation are emphasized much more in the case of the shear stress component, just because of its significantly smaller level. Despite these anomalies the influence of the shear imposed on the flow approaching the cylinder is clearly visible. The peak value of the $\langle u'v' \rangle$ stress component is increased by a factor of three or more.

Fig. 13 shows the pathlines extracted from the mean velocity field for two typical shear rates. The results for the other shear rates are similar to those in the case of the highest one. The goal was to explore the origin of the fluid elements which reside within the recirculation zone or flow through it. The pathlines were calculated by integrating back (against the flow directions) the positions of the fluid particles which ended up at the cross-section corresponding to the position $x/D = 0.5$. The pathline plot illustrates the fluid elements on the low velocity side flowing back to the cylinder in the presence of the high shear rate, whereas they recirculate within the separation bubble in the shearless case. Because the fluid elements on the low velocity side possess less momentum, the pressure gradient between the cylinder rear and the ambient wake can also be smaller (smaller pressure loss due to recirculation). This explains the higher base pressure (Figs. 15 and 16) by enhanced shear rates. The increase of the base pressure with the shear rate was also observed in the work of Cao et al. (2007).

Another useful illustration of the mean shear influence on the Reynolds stress field in the cylinder wake is given in form of the Reynolds stress anisotropy expressed by the stress anisotropy tensor $b_{ij} = \langle u_i u_j \rangle / (2k) - \delta_{ij}/3$ and its principal invariants, second $II = -b_{ij}b_{ij}/2$ and third $III = b_{ik}b_{kj}b_{ji}/3$. Fig. 14 shows the traces of the joint variations of $\xi = (III/2)^{1/3}$ and $\eta = (-II/3)^{1/2}$ in the anisotropy invariant map (Pope, 2000, scaled the principal invariants II and III in order to enhance the visibility) at the selected cross-section in the far wake at $x/D = 7$ from $y/D = -1.5$ to $y/D = 1.5$. The corresponding turbulence state resides very close to the right branch representing the axisymmetric turbulence. The maximum anisotropy (the point being closest to the one-component turbu-

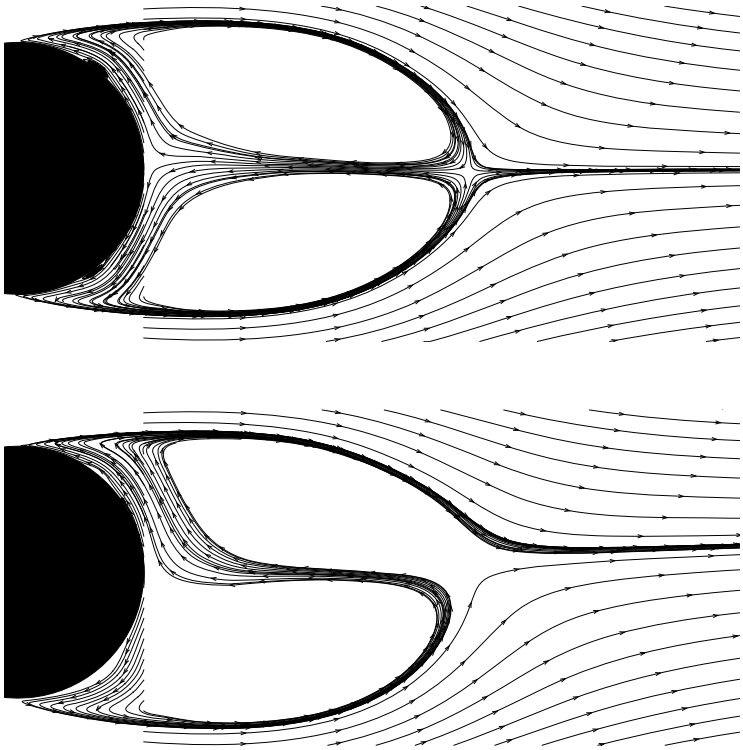

Fig. 13. Pathlines of the mean velocity field for different shear rates: SR = 0 (upper) and *0.177* (lower).

lence – upper right vertex – corresponding to the highest ξ and η values, approximatelly about $\geqslant 0.21$) is observed around the wake centerline ($y = 0$). Here, the normal Reynolds stress component $\langle v'v' \rangle$dominates over the other two (Fig. 9). In terms of the Reynolds stress anisotropy, the far wake behind cylinder is similar to the log-law region in the turbulent channel flow, whose turbulent state corresponds closely to the axisymmetric expansion (this is especially the case at very low Reynolds numbers). At the edges of the near wake (not shown here), the turbulence state deviates from the axisymmetric expansion towards the axisymmetric contraction. This trend was also observed in the developing region of the turbulent mixing layer in the experiment of Bell and Mehta (1990), despite the fact that the turbulent mixing layer is much less anisotropic than the turbulent cylinder wake. The difference between the shearless and the sheared configuration is only evident in the far wake. In the sheared case, the stress anisotropy is somewhat stronger on the high velocity side due to the shift of the Reynolds stress profiles (note the slight trend towards the central region of the invariant map represented by empty symbols in Fig. 14, lower). The strong bias in the shear Reynolds stress $\langle u'v' \rangle$ profile does not affect too much the stress anisotropy because $\langle u'v' \rangle$ is typically an order of magnitude smaller than the normal stress components.

3.2. Lift forces acting on cylinder

Fig. 15 compares the contours of the mean pressure field with and without velocity gradient imposed on the oncoming flow. The stagnation point at the upstream cylinder side is clearly shifted towards high velocity flow region, whereas the near wake structure remains nearly symmetrical. The mean pressure distributions on the cylinder for the shearless case and the case with the highest shear rate are shown in Fig. 16. The normalization was performed using the reference velocity U_∞ and reference pressure p_∞ at the inlet plane at $y/D = 0$ in accordance with the following formulation:

$$C_p = \frac{p - p_\infty|_{y=0}}{\frac{1}{2}\rho U_\infty^2|_{y=0}} \tag{7}$$

The angular position was measured clockwise from the stagnation point (intersection of the x-axis with the cylinder perimeter). Beside stagnation point displacement the pressure distribution indicates the surface pressure enhancement at the higher velocity side and decrease at the lower velocity side. Apart of that, the pressure coefficient variation reveals an almost entirely symmetrical distribution along the downstream cylinder surface ($|\theta| > 100°$). Another interesting observation is the base pressure coefficient increase in terms of the shear rate enhancement and the consequent drag coefficient decrease (not shown here).

In order to quantify the lift force acting on a cylinder, the lift coefficient C_l was examined. This coefficient is defined as follows:

$$C_l = \frac{F_l}{\frac{1}{2}\rho U_\infty^2|_{y=0} A} \tag{8}$$

where A is the projection area and F_l ($\equiv F_y$) is the cross component of the resultant force imposed on the cylinder consisting of the pressure and viscous forces:

$$F_i = -\int_A p\,\mathrm{d}A_i + \int_A \left(2\mu S_{ij} - \frac{2}{3}\mu\delta_{ij}S_{kk}\right)\mathrm{d}A_j; \quad i = x, y \tag{9}$$

Fig. 17 displays the time series plot of the lift coefficient C_l of the cylinder. The lift coefficient for SR = 0.177 is clearly shifted towards negative values in contrast to the shearless case, because of the displacement of the high pressure region observed in Fig. 15. This phenomenon corresponds to the particles' migration towards the side walls (i.e. towards negative velocity gradient) observed experimentally by Moraga et al. The Strouhal frequency f_{st}, extracted from the history of the lift coefficient, led to $St = 0.236$ for the shearless case. This value is somewhat higher compared to the relevant experimental investigation, e.g., Norberg (1987) – $0.21 \leqslant St \leqslant 0.22$ and Kwon et al. (1992) – $St = 0.22$. This departure is to the largest extent the consequence of a somewhat stronger flow acceleration over the cylinder due to the adopted flow domain height $H = 10D$ (Fig. 2), i.e. the blockage ratio $D/H = 0.1$, compared to the cases unaffected by the blockage through the upper and lower boundaries. Upper and lower solution domain boundaries (symmetry boundary conditions were applied here) are located at $y/D = 5$ and $y/D = -5$, respectively. It would be interesting here to repeat the conclusion from the workshop on LES of the flows past bluff bodies (Rodi et al., 1997) claiming that the prediction of the vortex shedding frequency should not be overvalued as the criteria for the quality of an LES simulation. The lift coefficients evaluated using Eq. (9) are summarized in Fig. 18 for all shear rates. For the sake of comparison, the lift coefficients obtained experimentally by Kato and Adachi (1976), Hayashi et al. (1991), Sumner and Akosile (2003) and Cao et al. (2007) are also displayed. The negative lift coefficient values being the consequence of the stagnation point dislocation at the windward side towards the upper cylinder half were clearly obtained for the entire shear rate range observed. A quantitative comparison is not entirely appropriate because of the significant differences in the flow Reynolds numbers these experimental investigations and

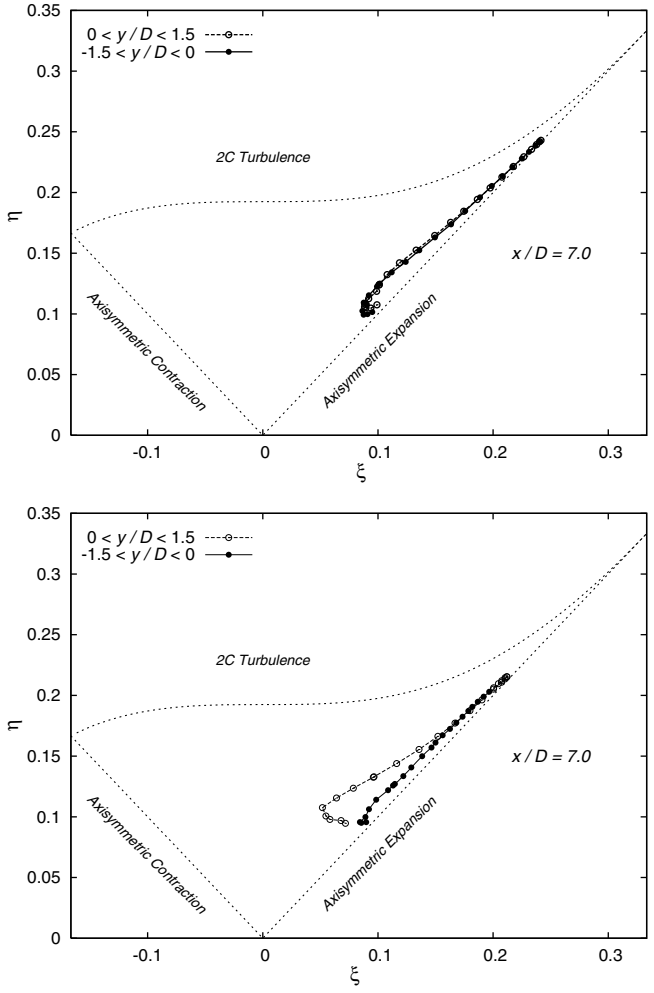

Fig. 14. Traces of joint variations of the second and third anisotropy invariants across the far wake at $x/D = 7.0$ for SR = 0 (upper) and SR = 0.177 (lower).

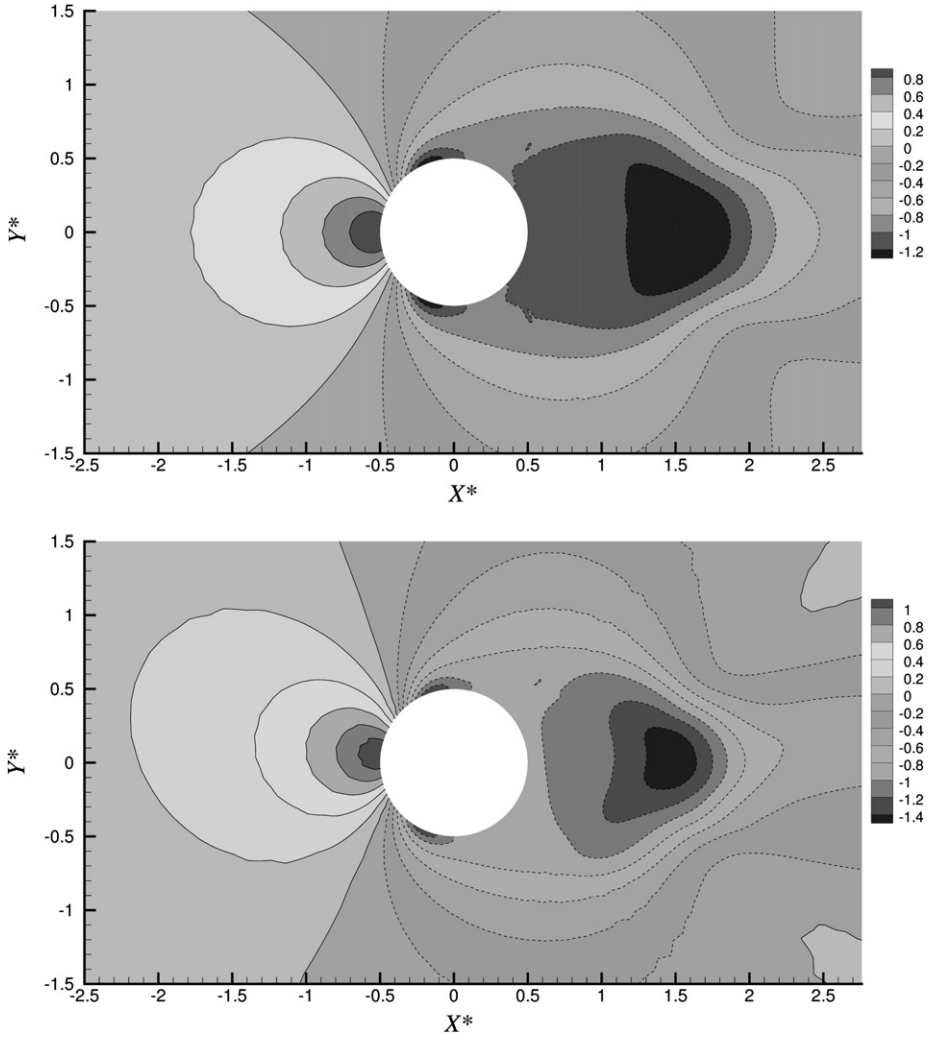

Fig. 15. Mean pressure field for SR = 0 (upper) and SR = 0.177 (lower). $X^* = x/D$, $Y^* = y/D$.

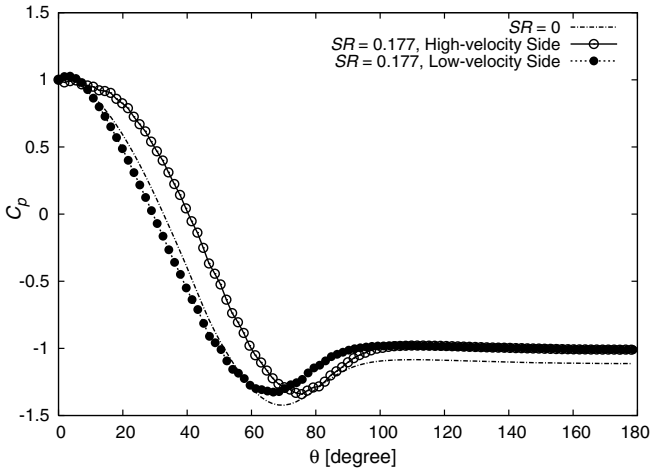

Fig. 16. Pressure coefficient distribution around cylinder.

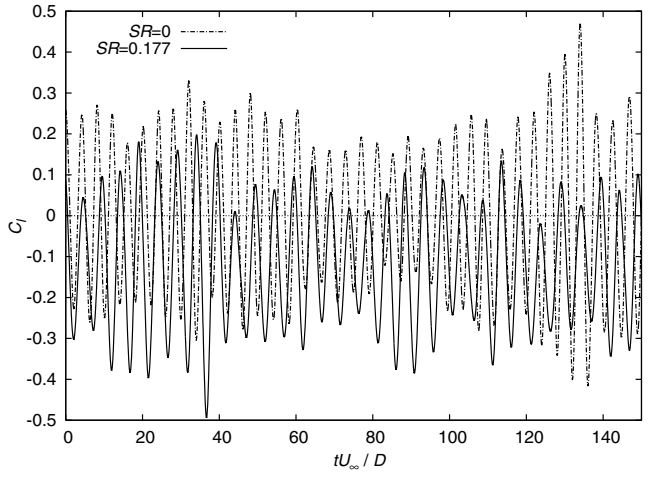

Fig. 17. Time series of the lift coefficient.

the present LES have been performed at (let us recall that all corresponding Reynolds numbers are still pertinent to the subcritical regime; see introductory section for their ranges). Nevertheless, the C_l variation with shear rate obtained in the present work follows closely the reference trend resulted from relevant experimental studies.

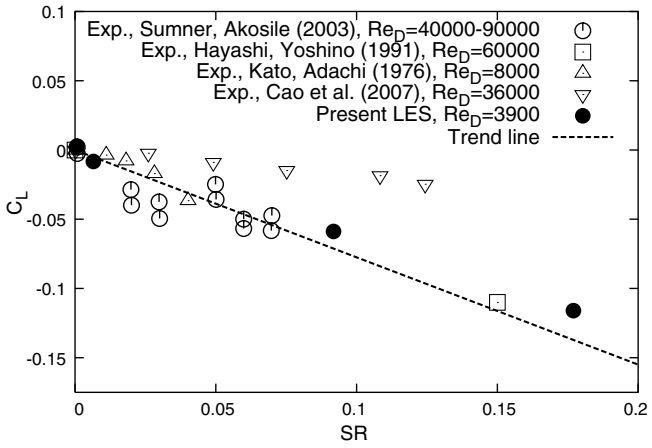

Fig. 18. Variation of the lift coefficient with shear parameter.

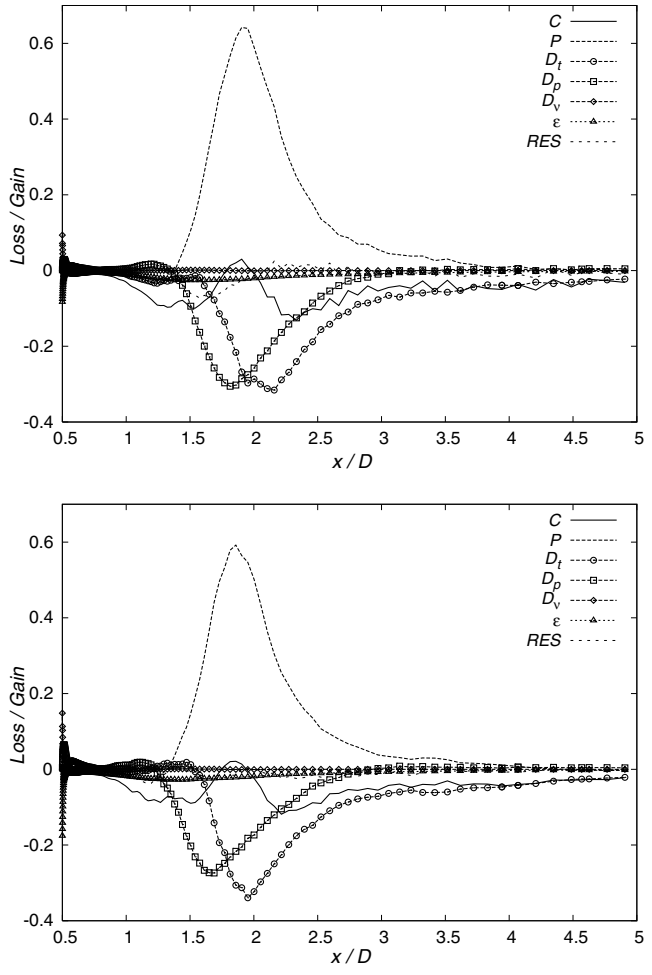

Fig. 19. Terms (normalized by U_∞^3/D) in budget of the equation of the kinetic energy of turbulence along the centerline in the cylinder wake $y/D = 0.0$ for SR = 0 (upper) and SR = 0.177 (lower).

3.3. Turbulence kinetic energy and Reynolds stress budgets

Important insight in the wake structure characteristics can be gained by studying the budgets of the terms in the equations governing the kinetic energy of turbulence ($k = 0.5\langle u_i' u_i' \rangle$) and the Reynolds stress components ($\langle u_i' u_j' \rangle$):

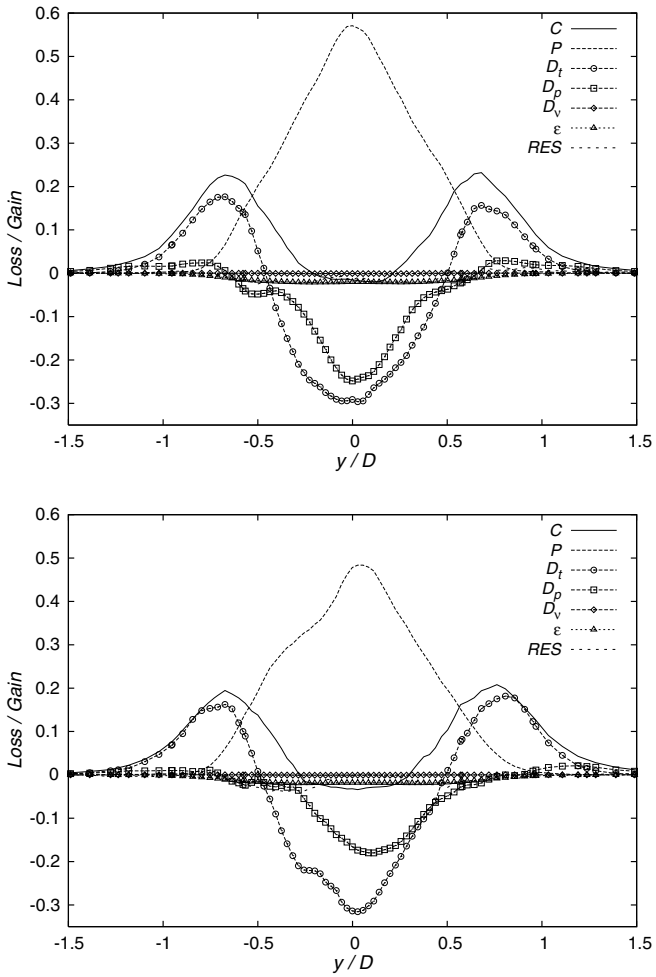

Fig. 20. Terms (normalized by U_∞^3/D) in budget of the equation of the kinetic energy of turbulence at $x/D = 2.0$ for SR = 0 (upper) and SR = 0.177 (lower).

$$\underbrace{\langle \overline{u}_k \rangle \frac{\partial \langle u_i' u_j' \rangle}{\partial x_k}}_{C_{ij}} = \underbrace{-\left(\langle u_k' u_i' \rangle \frac{\partial \langle \overline{u}_j \rangle}{\partial x_k} + \langle u_k' u_j' \rangle \frac{\partial \langle \overline{u}_i \rangle}{\partial x_k} \right)}_{P_{ij}} + \underbrace{\left\langle \frac{p'}{\rho} \left(\frac{\partial u_i'}{\partial x_j} + \frac{\partial u_j'}{\partial x_i} \right) \right\rangle}_{\Phi_{ij}}$$
$$\underbrace{-\frac{\partial \langle u_k' u_i' u_j' \rangle}{\partial x_k}}_{D_{ij}^t} \underbrace{-\frac{\partial}{\partial x_k} \left(\langle p' u_i' \rangle \delta_{jk} + \langle p' u_j' \rangle \delta_{ik} \right)}_{D_{ij}^p} \underbrace{+ \nu \frac{\partial^2 \langle u_i' u_j' \rangle}{\partial x_k^2}}_{D_{ij}^v}$$
$$\underbrace{-2\nu \left\langle \frac{\partial u_i'}{\partial x_k} \frac{\partial u_j'}{\partial x_k} \right\rangle}_{\epsilon_{ij}^{GS}}$$
$$\underbrace{-\frac{\partial \langle u_j' \tau_{ik}' + u_i' \tau_{jk}' \rangle}{\partial x_k}}_{D_{ij}^{SGS}} + \underbrace{\left\langle \tau_{ik}' \frac{\partial u_j'}{\partial x_k} + \tau_{jk}' \frac{\partial u_i'}{\partial x_k} \right\rangle}_{\epsilon_{ij}^{SGS}} \tag{10}$$

This equation is derived by manipulating appropriately the filtered Navier–Stokes equation and corresponding continuity equation (Eq. (2)). The last two terms on the right-hand-side (RHS) represent the contributions from the SGS stresses, one of which is of diffusive and the other of dissipative nature. The sum of the two dissipation terms, ϵ_{ij}^{GS} and ϵ_{ij}^{SGS}, is regarded as the stress energy dissipation rate ϵ_{ij}. The other terms are convection (C_{ij}), production (P_{ij}), redistribution (Φ_{ij}), turbulent diffusion (D_{ij}^t), pressure diffusion (D_{ij}^p) and molecular (viscous) diffusion (D_{ij}^v). The transport equation of the turbulence kinetic energy k can be easily obtained by contracting the indices ($i = j$). It should be recalled that the budgets of the Reynolds stress equations obtained from a large eddy simulation can differ from the true budgets because of the filtering operation being

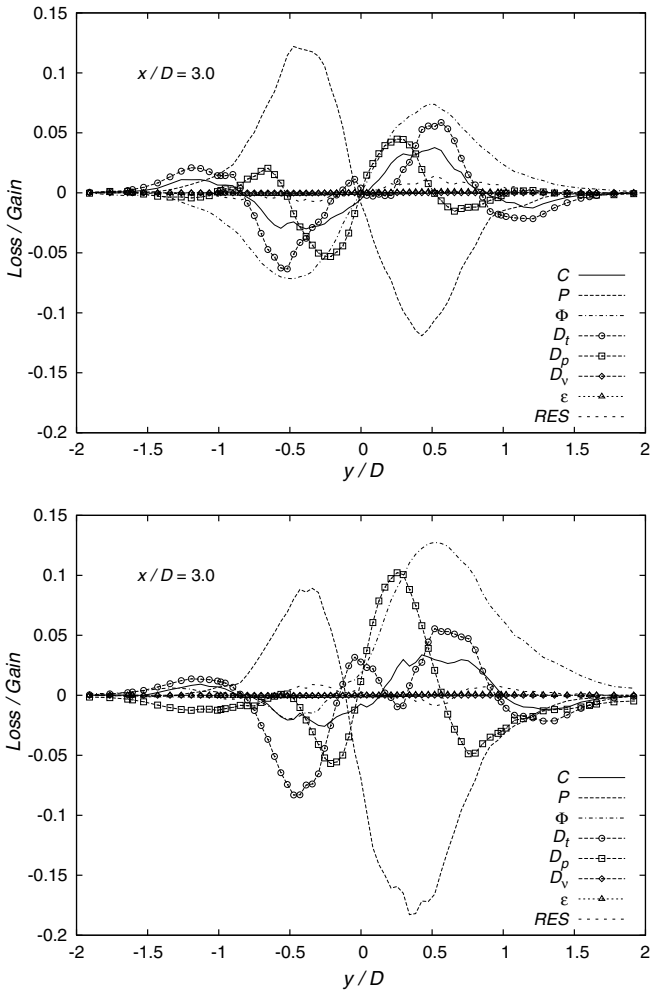

Fig. 21. Terms (normalized by U_∞^3/D) in budget of the equation of the Reynolds shear stress at $x/D = 3.0$ for SR = 0 (upper) and SR = 0.177 (lower).

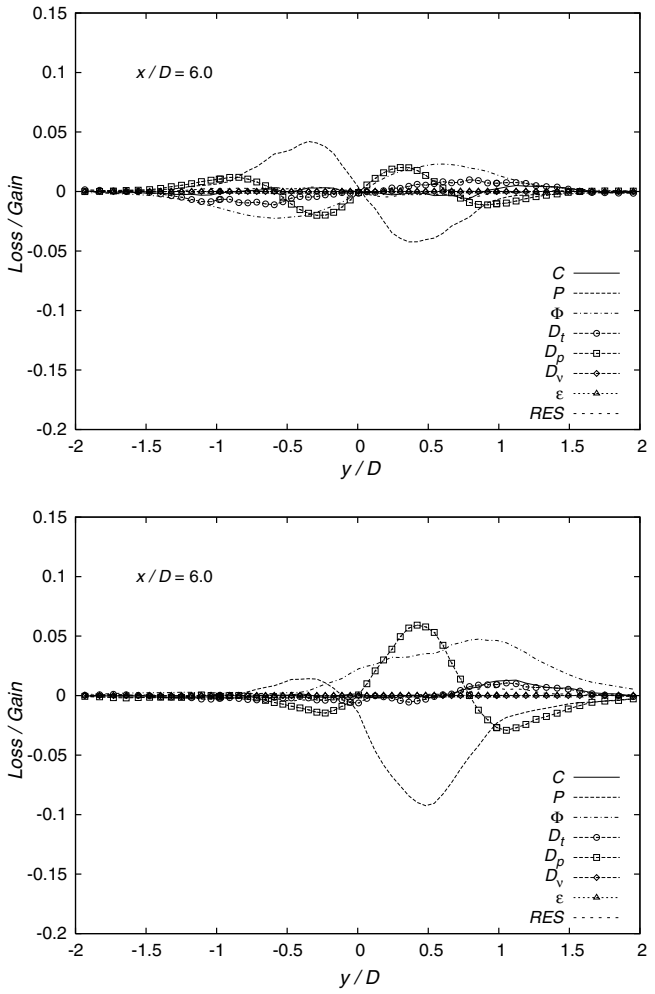

Fig. 22. Terms (normalized by U_∞^3/D) in budget of the equation of the Reynolds shear stress at $x/D = 6.0$ for SR = 0 (upper) and SR = 0.177 (lower).

inherently contained in the LES method. However, the effect of the filtering in this study is considered to be rather limited to the dissipation term, since the grid filter is placed well in the inertial subrange. Another important remark to be made is that when using an eddy viscosity type model, $\tau_{ij}^a = \tau_{ij} - \delta_{ij}\tau_{kk}/3 = -2\nu_t\overline{S}_{ij}$, the computationally obtained pressure represents actually the modified pressure

$$\overline{P} = \overline{p} + \frac{\rho}{3}\tau_{kk}; \quad P' = p' + \frac{\rho}{3}\tau'_{kk} \tag{11}$$

whose effect on the evaluation of the terms in Eq. (10) comprising pressure is also considered to be negligible, because the SGS kinetic energy $\tau_{kk}/2$ is only a fraction of the total turbulent kinetic energy as illustrated in Fig. 5. In the following, the symbol for the filter operation ($\overline{(\ )}$) is omitted for the sake of simplicity.

Fig. 19 shows the evolution of the terms in the turbulent kinetic energy budget along the centerline $y = 0$ in the near wake for both the shearless and the sheared cases. The residual of the balance equation, being sufficiently small, is denoted as 'RES'. Fig. 19 reveals high similarity level, even quantitatively, in the dynamics of the corresponding turbulent mechanisms for both cases. The production term ($P_{kk}/2$) reaches its maximum around the free reattachment point ($x/D \approx 1.8$). The reattachment region represents a region, where the upper and lower separated shear layers impinge onto each other. This stagnation flow region is characterized by intensive straining contributing strongly to the enhanced turbulence production. Afterwards the mean velocity gradients at the symmetry plane, and consequently the production rate, weaken gradually towards zero value in the very far wake. The difference between the production term and the two diffusion terms, the pressure diffusion term ($D_{kk}^p/2$) and the turbulent diffusion term ($D_{kk}^t/2$), is balanced by the convection transport (solid line), which represents the rate of change of the turbulence kinetic energy along the streamline. It should be noted here, that the convective term, in contrast to the other terms, acts on the left-hand-side (LHS) of Eq. (10). Immediately after the recirculation zone characterized by a low intensity flow reversal the diffusive transport terms reached their peak values corresponding to the production rate maximum. In the recovery region after the reattachment, the kinetic energy production is mainly balanced by the turbulent diffusion and convective transport. The dynamics of the turbulent kinetic energy transport immediately after the reattachment, shown in Fig. 20, reveals the entirely symmetric profile shapes pertinent to all budget terms for both sheared and shearless cases. This is consistent with the behaviour of the normal Reynolds stress components, which are only slightly affected by the imposed mean shear and retain almost symmetrical profile in the near wake, Fig. 12. In both cases investigated, the turbulent kinetic energy production is highest in the wake core. The same is valid for both diffusion processes (D_{kk}^t and D_{kk}^p) which completely balance the production rate in this central region. In the edge regions of the wake ($\pm 0.5 < y/D < \pm 1.0$) the both transport processes, turbulent diffusion and convection, dominate the turbulence dynamics. The same remark concerning the sign of the convective term in the dis-

cussion above (related to Fig. 19 and Eq. (10)) applies here too. The importance of the diffusion process in this free flow should be underlined at this place. Unlike in the wall-bounded flows, e.g. channel flow (Mansour et al., 1988), where the diffusion transport (it relates to both terms D^t_{kk} and D^p_{kk}) plays a secondary role, it dominates the turbulence kinetic energy budget (the same is valid for the individual Reynolds stress components).

The budgets of the normal Reynolds stress components ($\langle u'u'\rangle$, $\langle v'v'\rangle$ and $\langle w'w'\rangle$) follow a similar symmetrical pattern and are only slightly influenced by the mean shear. Because of that, they are not shown here. The interested readers are referred to the work of Omori (2007). It should be only noted, that the production and the pressure diffusion processes are absent in the budget of the spanwise stress component, because of the statistical homogeneity of the flow. The energy, fed into this component from the other two stresses by the redistribution mechanism, is simply dissipated and transported to the wake edges by the turbulent diffusion process. The convective transport development points out the maximum value of $\langle w'w'\rangle$in the reattachment region.

The most important difference between the shearless and the sheared cases is observed in the dynamics of the shear stress component, as presumed from Fig. 12. Figs. 21 and 22 compare the Reynolds shear stress ($\langle u'v'\rangle$) budgets along the cross-section at two selected locations in the wake: $x/D = 3.0$ (immediately after reattachment, where the $\langle u'v'\rangle$ stress component exhibits sign change towards negative values in the upper wake half, Figs. 9 and 12) and $x/D = 6.0$ (corresponding to far wake, where the $\langle u'v'\rangle$ stress takes only positive values, Fig. 12) for the shearless case and the most strongly sheared case. In both cases, the essential transport mechanism is qualitatively similar. Unlike in the budgets of the kinetic energy of turbulence and all three normal stress components, the influence of the mean shear on the shear stress structure is clearly evident. The maxima and minima of the production term are located in the shear layer, i.e. the edge region of the wake $y/D \approx \pm 0.5$. This location coincides with the peak values of the shear stress component itself. The production term is mostly in balance with the redistribution term in both cases. However, its effect is totally different. While for the shearless case, the redistribution term acts to reduce the level of the Reynolds shear stress, hence the anisotropy, for the sheared case, the redistribution term behaves in fact as the production term increasing the Reynolds shear stress and consequently causes the shift of other stress components (Fig. 12). The diffusion terms exhibit a unique alternating pattern in accordance with the antisymmetric distribution of $\langle u'v'\rangle$. The diffusion process, especially the one driven by the fluctuating pressure (D^p_{12}), is enhanced in the upper half of the wake and attenuated in its lower half. This phenomenon, in addition to the convection due to the fluid entrainment observed in Fig. 13, is believed to have important contribution in driving the shift of the Reynolds stress profiles (Fig. 12). The peak value locations of the convective term, being actually situated on the LHS of Eq. (10) (representing accordingly its imbalance), coincide with the maxima/minima positions of the other terms. What is particular with the strong asymmetry of the shear Reynolds stress is the significant enhancement of its positive value in the entire wake region downstream the location $x/D \approx 4.0$ being in accordance with the coherent structure intensification on the high velocity side, observed in Fig. 24. Admittedly, a certain doubt concerning the credibility of the budget evaluation can arise, keeping in mind the anomalous dimples at the shear stress profiles, Figs. 9 and 12. We would like to emphasize that the $\langle u'v'\rangle$budget was obtained by evaluating the terms in the corresponding exact transport equation (Eq. (10)). No single term in this equation is dependent on the (time-averaged) shear stress component, not even the production

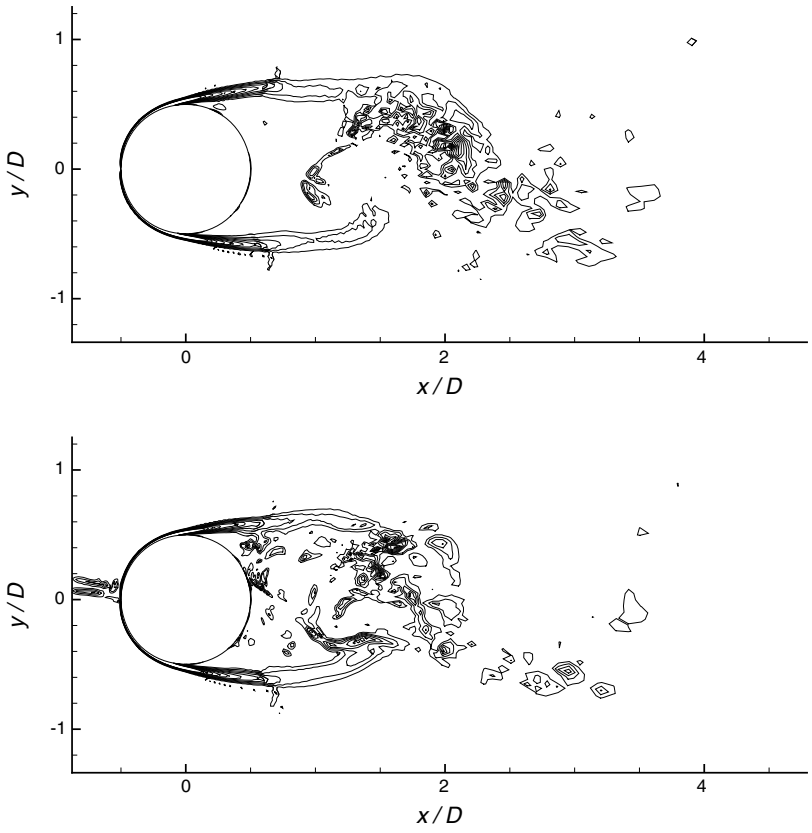

Fig. 23. Spanwise vortex structures in the near wake: 11 contours of instantaneous vorticity magnitude between $|\omega_z|D/U_\infty = 2.5$ and $|\omega_z|D/U_\infty = 10.0$ for SR = 0 (upper) and SR = 0.177 (lower).

term: $P_{12} = -\langle u'u'\rangle\partial\langle V\rangle/\partial x - \langle u'v'\rangle(\partial\langle U\rangle/\partial x + \partial\langle V\rangle/\partial y) - \langle v'v'\rangle\partial\langle U\rangle/\partial y$. The term in brackets corresponds to the divergence of the mean velocity field which takes zero value in the case of incompressible flow considered here. Accordingly the evaluation of the $\langle u'v'\rangle$budget is not influenced by the anomalous $\langle u'v'\rangle$ profile.

3.4. Wake structure visualization

The cylinder wake and its structural characterization have important impact on the forces acting on cylinder. Fig. 23 shows the contours of the instantaneous spanwise vorticity ω_z in the near wake of both shearless and sheared cases. Eleven contours of instantaneous vorticity magnitude between $|\omega_z|D/U_\infty = 2.5$ and $|\omega_z|D/U_\infty = 10.0$ are displayed. The snapshots were made at the time instant, where the lift coefficient reached its minimum. In both flow configurations, the boundary layer separating from the cylinder surface and the consequent development of the Kármán vortex street are clearly promoted. The onset of the laminar-to-turbulent transition in the shear layer is also noticeable as well as the intensification of the turbulent fluctuations entrainment into the separation bubble. In the sheared case, the shear layer on the lower side tends to be drawn back to the cylinder. This case is characterized by more detailed small structures immediately behind the cylinder.

Further illustration of the mean shear influence on the coherent structures in the cylinder wake is given in Fig. 24, where the iso-surfaces of the pressure fluctuations at one instant were compared for three shear rates. The level of each iso-surface was common for

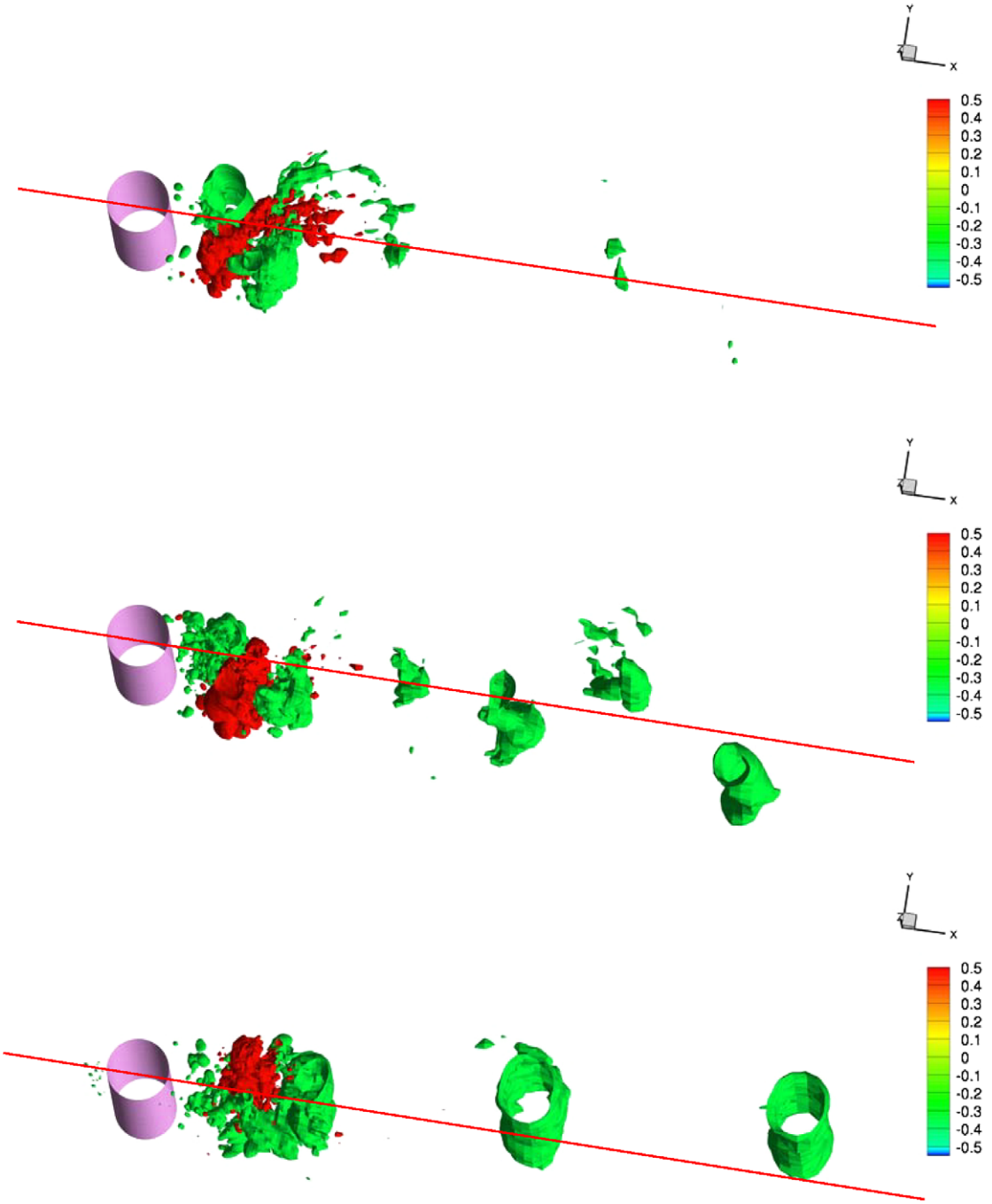

Fig. 24. Iso-surfaces (three levels) of the pressure fluctuation (from the top: SR = 0, 6.53 × 10^{-4}, 1.77 × 10^{-1}).

all three cases. Regions of alternating, regularly located negative and positive pressure regions, which indicate the existence of the Kármán vortices, can be seen in all three cases. However, intensification of the asymmetry with the shear rate is especially visible when comparing the last two figures. In the far wake, the vortex formation doesn't follow a staggered arrangement on both sides of the cylinder at the highest shear rate, in contrast to the case characterized by a fairly weak shear rate (SR = 0.000653). Accordingly, the vortices are observed only on the high velocity side. Regardless of the level of the iso-surface, no coherent structures on the low velocity side were recognized. In the case of higher shear rates, the vortices are well preserved even in the far wake region. The convection into the positive y direction is clearly intensified, contributing decisively to the enhancement of the positive shear stress component (Figs. 21 and 22).

The vortex structure in the wake is further represented by means of the Q-criterion ($Q = 0.5(\Omega_{ij}\ \Omega_{ij} - S_{ij}\ S_{ij})$), representing in general the second invariant of the velocity gradient tensor, Hunt et al. (1988). With this criterion the influence of the mean shear imposed on inflow on the small scales in the wake can be investigated. As illustrated in Fig. 25, the small vortical structures connecting the large-scale vortices exhibit no significant differences between the shearless and sheared cases. It can be inferred that the small-scale motion in the wake is less affected by the mean shear than the large-scale motion, the latter observation being reflected in the mean velocities and the second moments. The spanwise length scale of the small structures in the near wake is typically one fourth to one third of the cylinder diameter, which is in good agreement with the experimental and numerical observations found in the open literature, see e.g., the works of Kravchenko and Moin (2000), Mansy et al. (1994) and Williamson (1996).

4. Conclusions

Turbulent flow past a circular cylinder subjected to uniform mean shear at Reynolds number $Re_D = 3900$ was studied computationally by means of large eddy simulation (LES) in the range of shear rates SR between 0 and 0.177. Special attention was devoted to minimizing the uncertainties arising from the grid quality and the adopted grid resolution and the imposed boundary conditions were assessed in detail. The focus of the present work was on the wake structure. In the very near wake, the inlet mean shear caused the entrainment of the fluid elements into the recirculation bubble on the low velocity side. This process is responsible for the pressure loss reduction, but the turbulence statistics remain almost unaffected in this flow region. The symmetric profile shapes were preserved. In contrast, in the wake region after reattachment the mean flow statistics were shifted to the high velocity side by increasing the shear rate. The analysis of the stress anisotropy revealed that the turbulence structure closely followed the axisymmetric expansion state. The strongest influence of the mean shear was observed in the profiles of the turbulent shear stress $\langle u'_1 u'_2 \rangle$, whose positive value enhancement was mostly caused by the fluctuating pressure-related turbulent mechanisms. The $\langle u'_1 u'_2 \rangle$ energy budget exhibits an asymmetrical distribution,

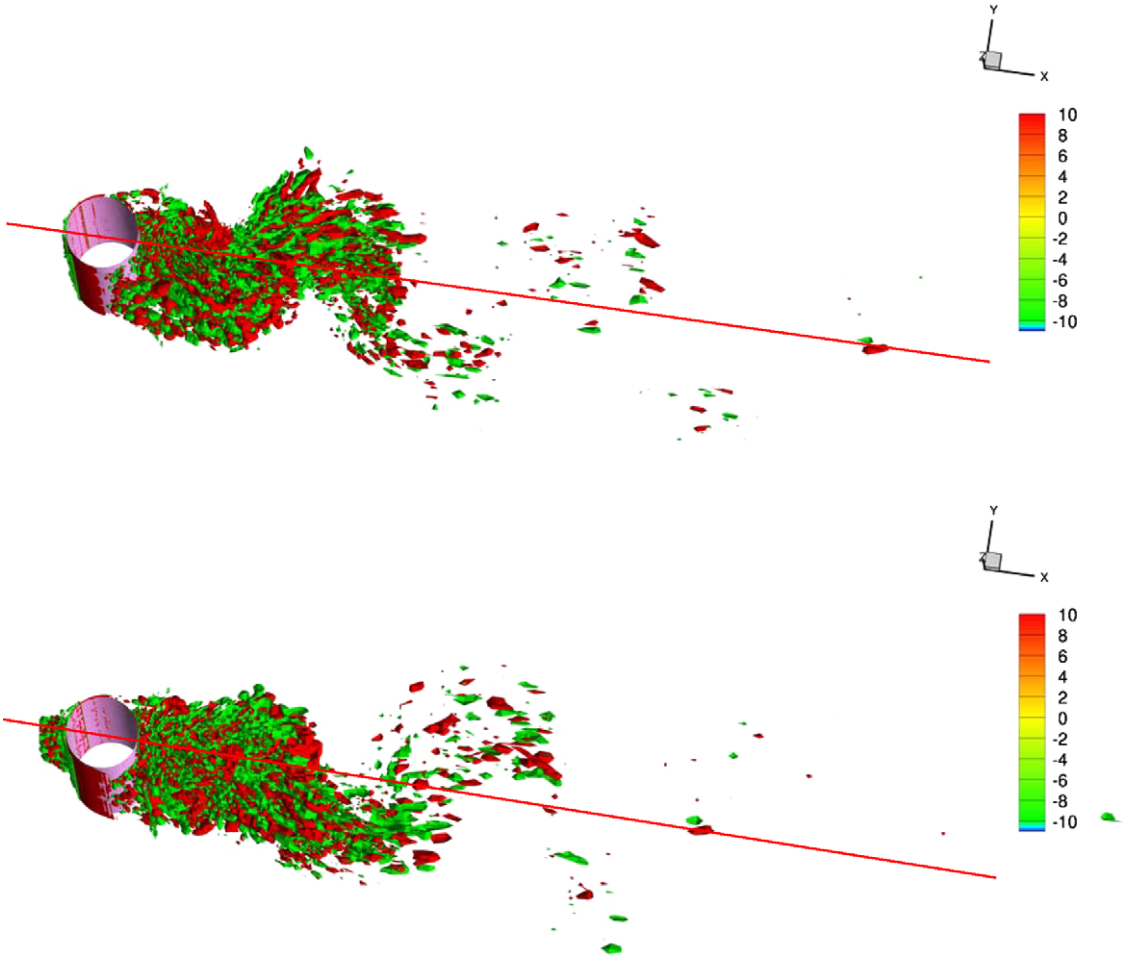

Fig. 25. Iso-surfaces (two levels) of Q: SR = 0 (upper) and 0.177 (lower); note the inclined x-axis.

promoting the asymmetry of the normal turbulent stress components and formation of coherent structures on the high velocity side. The lift force pushing the cylinder towards negative mean velocity gradient is the consequence of the asymmetric pressure distribution characterized by the displacement of the stagnation point on the windward side. The increase of the negative lift coefficient in terms of the shear rate obtained computationally is supported by the reference experimental investigations.

Acknowledgements

The financial support of the German Academic Exchange Service (DAAD) for T. Omori is gratefully acknowledged. We are grateful to the reviewers for numerous specific comments and suggestions.

References

Akagawa, K., Fuji, T., Takenaka, N., 1989. The effects of the density ratio in a vertically rising solid–liquid two-phase flow. In: Proceedings of the International Conference on Mechanics of Two-Phase Flows, Teipei, Taiwan, pp. 203–208.

Bell, J.H., Mehta, R.D., 1990. Development of a two-stream mixing layer from tripped and untripped boundary layers. AIAA J. 28 (12), 2034–2042.

Beaudan, B., Moin, P., 1994. Numerical experiments on the flow past a circular cylinder at a sub-critical Reynolds number. Technical Report TF-62, Thermosciences Division, Department of Mechanical Engineering, Stanford University.

Breuer, M., 1998. Large eddy simulation of the subcritical flow past a circular cylinder: numerical and modeling aspects. Int. J. Numer. Methods Fluids 28, 1281–1302.

Cao, S., Ozono, S., Hirano, K., Tamura, Y., 2007. Vortex shedding and aerodynamic forces on a circular cylinder in linear shear flow at subcritical Reynolds number. J. Fluids Struct. 23, 703–714.

Cheng, M., Tan, S.H.N., Hung, K.C., 2005. Linear shear flow over a square cylinder at low Reynolds number. Phys. Fluids 17, 078103.

FASTEST-Manual, 2005. Department for Numerical Methods in Mechanical Engineering, Darmstadt University of Technology.

Germano, M., Piomelli, U., Moin, M., Cabot, W.H., 1991. A dynamic subgrid-scale eddy viscosity model. Phys. Fluids A 3 (7), 1760–1765.

Hayashi, T., Yoshino, F., Waka, R., 1991. An analytical evaluation of the aerodynamic forces acting on a circular cylinder in a uniform shear flow. In: Morris et al. (Eds.), Proceedings of the 1st ASME/JSME Fluid Engineering Conference, FED, vol. 112, Portland, OR, pp. 83–88.

Hinze, J.O., 1975. Turbulence, second ed. McGraw Hill, New York.

Hunt, J.C.R., Wray, A.A., Moin, P., 1988. Eddies, streams and convergence zones in turbulent flows. Technical Report CTR-S88, Center for Turbulence Research, Stanford University.

Kato, E., Adachi, T., 1976. An effect of the velocity gradient of main flow on vortex shedding from a circular cylinder (in Japanese). Trans. Jpn. Soc. Aeronaut. Space Sci. 24 (270), 333–341.

Kravchenko, A.G., Moin, P., 2000. Numerical studies of flow over a circular cylinder at $Re_D = 3900$. Phys. Fluids 12 (2), 403–417.

Kwon, T.S., Sung, H.J., Hyun, J.M., 1992. Experimental investigation of uniform shear flow past a circular cylinder. ASME J. Fluids Eng. 114, 457–460.

Lourenco, L.M., Shih, C., 1993. Characteristics of the plane turbulent near wake of a circular cylinder, a particle image velocimetry study, Private communication in Kravchenko and Moin 2000. Phys. Fluids 12 (2), 403–417.

Lilly, D.K., 1992. A proposed modification of the Germano subgrid-scale closure method. Phys. Fluids A 4 (3), 633–635.

Luo, S.C., Tong, X.H., Khoo, B.C., 2007. Transition phenomena in the wake of a square cylinder. J. Fluids Struct. 23, 227–248.

Mansour, N.N., Kim, J., Moin, P., 1988. Reynolds-stress and dissipation-rate budgets in a turbulent channel flow. J. Fluid Mech. 194, 15–44.

Mansy, H., Yang, P.M., Williams, D.R., 1994. Quantitative measurements of three-dimensional structures in the wake of a circular cylinder. J. Fluid Mech. 270, 277–296.

Mason, P.J., Callen, N.S., 1985. On the magnitude of the subgrid-scale eddy coefficient in large-eddy simulation of turbulent channel flow. J. Fluid Mech. 162, 439–462.

McLaughlin, J.B., 1991. Inertial migration of a small sphere in linear shear flow. J. Fluid Mech. 224, 261–274.

McLaughlin, J.B., 1993. The lift on a small sphere in wall-bounded linear shear flow. J. Fluid Mech. 246, 249–265.

Mei, R., 1992. An approximate expression for the shear lift force on a spherical particle at finite Reynolds number. Int. J. Multiphase Flow 18 (1), 145–147.

Mittal, R., Moin, P., 1997. Suitability of upwind-biased finite-difference schemes for large-eddy simulation of turbulent flows. AIAA J. 35, 1415–1417.

Moraga, F.J., Bonetto, F.J., Lahey, R.T., 1999. Lateral forces on spheres in turbulent uniform shear flow. Int. J. Multiphase Flow 25, 1321–1372.

Norberg, C., 1987. Effects of Reynolds number and a low-velocity free-stream turbulence on the flow around a circular cylinder. Technical Report No. 87/2, Chalmers University of Technology, Sweden.

Omori, T., 2007. LES study of flow past a cylindrical particle subjected to mean shear. Ph.D. Thesis, Darmstadt University of Technology.

Ong, L., Wallace, L., 1996. The velocity field of the turbulent very near wake of a circular cylinder. Exp. Fluids 20, 441–453.

Parnaudeau, P., Heitz, D., Lamballais, E., Silvestrini, J.H., 2007. Direct numerical simulations of vortex shedding behind cylinders with spanwise linear nonuniformity. J. Turbulence 8 (13).

Piomelli, U., Chasnov, J., 1996. Large-eddy Simulations: Theory and Applications. Kluwer Academic Publisher.

Pope, S.B., 2000. Turbulent Flows. Cambridge University Press, Cambridge, UK.

Rodi, W., Ferziger, J.H., Breuer, M., Pourquié, M., 1997. Status of large eddy simulation: results of the workshop on LES of flows past bluff bodies. J. Fluids Eng. 119 (2), 248–262.

Roshko, A., 1954. On the development of turbulent wakes from vortex streets NACA-TN 1191.

Saffman, P.G., 1965. The lift force on a small sphere in a slow shear flow. J. Fluid Mech. 22, 385–400.

Saffman, P.G., 1968. Corrigendum to "The lift force on a small sphere in a slow shear flow". J. Fluid Mech. 31, 624.

Sakaguchi, T., Shakutsi, H., Tomiyama, A., Minigawa, A., Kitani, H., 1991. Microscopic characteristics of multiphase flow using digital image processing. In: Proceedings of The International Conference on Multiphase Flows, Tsukuba, Japan, pp. 357–360.

Schlichting, H., 1979. Boundary-Layer Theory, seventh ed. McGraw Hill Inc., New York.

Sumner, D., Akosile, O.O., 2003. On uniform planar shear flow around a circular cylinder at subcritical Reynolds number. J. Fluids Struct. 18, 441–454.

Tavoularis, S., Stapountzis, H., Karnik, U., 1987. Vortex shedding from bluff cylinders in strongly sheared turbulent streams. J. Wind Eng. Indus. Aerodyn. 26 (2), 165–178.

Travin, A., Shur, M., Strelets, M., Spalart, P., 1999. Detached-eddy simulations past a circular cylinder. Flow Turbulence Combust. 63, 293–313.

Tremblay, F., 2001. Direct and large-eddy simulation of flow around a circular cylinder at subcritical Reynolds numbers. Ph.D. Thesis, Technical University Munich, Germany.

Wang, Q., Squires, K.D., Chen, M., McLaughlin, J.B., 1997. On the role of the lift force in turbulence simulations of particle deposition. Int. J. Multiphase Flow 23 (4), 749–763.

Williamson, C.H.K., 1996. Vortex dynamics in the cylinder wake. Annu. Rev. Fluid. Mech. 28.

Woo, H.G., Cermak, J.E., Peterka, J.A., 1989. Secondary flows and vortex formation around a circular cylinder in constant shear flow. J. Fluid Mech. 204, 523–542.

Zdravkovich, M.M., 1997. Flow Around Circular Cylinders: Fundamentals. Oxford Science Publications.